Temporal and Spatial Characteristics of AIRS and CERES OLR Climatologies and Anomaly Time Series

Joel Susskind, NASA Goddard Space Flight Center

Jae N. Lee, Joint Center for Earth Systems Technology, University of Maryland, Baltimore County

Lena Iredell, ADNET

Norman G. Loeb, NASA Langley Research Center

Key Points

This paper compares the temporal and spatial characteristics of the monthly mean AIRS Version-6 OLR and CERES EBAF_Edition 4.0 OLR data sets over the period 2003 through 2016.

AIRS OLR displays a positive global mean bias as compared to CERES OLR of approximately 3.0 W/m^2 that is essentially constant in space and time.

There is excellent agreement between the spatial distributions of monthly mean AIRS and CERES OLR climatologies, as well as of the trends of the AIRS and CERES OLR anomaly time series and their correlations with an El Niño Index. The largest AIRS/CERES OLR differences occur in places where diurnal differences of AIRS OLR are largest.

This agreement also validates the AIRS retrieved geophysical parameters. These geophysical parameters help explain the factors influencing OLR variability.

Abstract

This paper compares the characteristics of the monthly mean AIRS Version-6 and CERES_EBAF Edition 4.0 OLR data sets over a 14-year overlap period, September 2002 through August 2016. These comparisons include spatial plots of monthly mean OLR climatologies and spatial plots of OLR Average Rates of Change (ARCs), representative of the slopes of the linear least squares fits to anomaly time series. This paper also compares spatial plots of El Niño Correlations (ENCs) of the AIRS OLR and CERES OLR anomaly time series. ENCs represent temporal correlations of anomaly time series with an El Niño Index that we define in this paper. In addition, we show ARCs and ENCs of select derived AIRS geophysical parameters that help explain OLR variability in space and time.

AIRS flies on EOS Aqua. There are separate AIRS data sets that use data observed only in ascending Aqua orbits ($AIRS_{PM}$) and data observed only in descending Aqua orbits ($AIRS_{AM}$). An additional data set of AIRS products exists based on observations made in both orbits ($AIRS_{AVG}$). There is excellent agreement between the ARCs of CERES OLR and the ARCs of $AIRS_{AVG}$ OLR down to the 1˚ latitude by 1˚ longitude spatial scale. The $AIRS_{AVG}$ OLR product displays a positive global mean monthly mean bias compared to CERES OLR of roughly 3.0 W/m^2 that is essentially constant in space and time. The largest differences between $AIRS_{AVG}$ OLR and CERES OLR monthly climatologies and anomaly time series occur in regions where the diurnal differences of AIRS OLR are largest.

AIRS OLR and CERES OLR are independent products. The agreement between the AIRS OLR and CERES OLR data sets therefore serves to validate both OLR data sets and indicates that neither data set contains spurious drifts. The agreement between the AIRS OLR and CERES OLR data sets also validates, to some extent, values and short-term trends of the AIRS retrieved geophysical parameters used in the computation of AIRS OLR. The temporal and spatial variability of AIRS retrieved geophysical parameters help explain those of OLR.

1.0 Introduction

This paper compares monthly mean values of the AIRS Version-6 Outgoing Longwave Radiation (OLR) data set and the CERES_EBAF Edition 4.0 OLR data set over a 14-year overlap period, September 2002 through August 2016. OLR, the residual between incoming solar radiation and the sum of outgoing longwave (LW) and reflected shortwave (SW) radiation, is an important component of the Earth's energy imbalance. The Earth's climate will warm or cool depending on the sign and magnitude of its energy imbalance.

Chu and Wang (1997), Soden and Held (2006), Soden et al. (2008), Dessler et al. (2008), Huang and Ramaswamy (2009), Chung et al. (2010), Dessler (2010), Zelinka and Hartmann (2011), Zelinka et al. (2012a), (2012b), and Vonder Haar et al. (2012) utilized the spatial and temporal variability of OLR in their studies of climate processes. Kidson et al. (2002), Jones et al. (2004), Barlow et al. (2005), Kiladis et al. (2005), Hoyos and Webster (2007), Wong et al. (2006), Chiodi and Harrison (2010), Tian et al. (2010), Loeb et al. (2012), and Hartmann and Ceppi

(2013) all used OLR variability as a proxy for tropical convective activity to further their understanding of climate processes. The new AIRS OLR and CERES OLR data sets described in this paper provide an improved depiction to scientists of the variability of OLR over the fourteen-year period under study. Other AIRS products help to explain this variability in terms of the variability surface and atmospheric parameters during this time-period.

Susskind et al. (2012) compared values of the monthly mean AIRS Version-5 OLR data set, including anomaly time series over the period September 2002 through June 2011, with analogous results contained in the CERES Edition 2.6r OLR data set. Susskind et al. (2012) showed that while there were biases between the AIRS OLR and CERES OLR monthly mean data sets they used, the AIRS OLR and CERES OLR anomaly time series, including short-term trends over the period September 2002 through June 2011, matched each other very closely on a 1°x1° spatial scale.

Following the methodology of Susskind et al. (2012), this paper compares ARCs (Average Rates of Change) and ENCs (El Niño Correlations) of AIRS OLR anomaly time series with those of CERES OLR. The ARC of an anomaly time series is the slope of the linear least squares fit to the anomaly time series over the time-period under study, and the ENC of an anomaly time series is its temporal correlation with an El Niño Index (ENI). Susskind et al. (2012) defined the ENI as the difference of the NOAA monthly mean oceanic Sea Surface Temperature (SST), averaged over the NOAA Niño-4 spatial region extending from 5°N to 5°S longitude and from 160°E eastward to 150°W, from an eight year climatology which Susskind et al. (2012)

generated. This paper redefines the ENI with regard to both the spatial and time domains. We now define the ENI to include the average NOAA SST anomalies over the combined Niño-4 and Niño-3 spatial regions, again extending from 5°N to 5°S latitude and now extending from 160°E longitude further eastward to 90°W longitude. We further extended the spatial domain of the ENI in this paper because the center of El Niño/La Niña activity shifted eastward into the Niño-3 spatial domain over the latter part of the fourteen-year time-period under study. We now define monthly mean values of the ENI, as well as anomalies of all geophysical parameters, as monthly mean differences from their fourteen-year climatologies.

This paper differs from in Susskind et al. (2012) in two very important ways regarding the data sets used. AIRS flies on EOS Aqua and takes observations in ascending orbits nominally at 1:30 PM local time and in descending orbits nominally at 1:30 AM local time. Separate $AIRS_{PM}$ and $AIRS_{AM}$ data sets exist based on observations made only in those orbits. Susskind et al. (2012) only examined characteristics of an AIRS OLR data set derived using observations taken on both sets of orbits. In this paper, we examine characteristics of $AIRS_{PM}$ and $AIRS_{AM}$ data sets separately, as well as characteristics of a data set derived using observations taken on both sets of orbits, $AIRS_{AVG,}$ as done by Susskind et al. (2012). In addition, we now use the improved AIRS and CERES OLR data sets, AIRS/AMSU Version-6 and CERES_EBAF (Energy Balanced and Filled) Edition 4.0.

The methodology used to produce CERES_EBAF Edition 4.0 OLR involves combining CERES observations on the Terra and Aqua satellites with imager observations from

Geostationary (GEO) satellites in order to account for hourly Top_of_Atmosphere (TOA) flux variations throughout the day in every region over an entire month (Doelling et al., 2013; Loeb et. al., 2018). The AIRS Version-6 OLR product uses observations taken only in the Aqua orbit. Consequently, even with perfect AIRS and CERES OLR data products, one would still expect differences between the $AIRS_{AVG}$ OLR data set and the CERES OLR data set resulting from differences in temporal sampling. This is especially true over land in locations in which Aqua does not sample during times of maxima and minima of either land surface skin temperature or of convection. The $AIRS_{PM}$ OLR and $AIRS_{AM}$ OLR data sets show areas, especially over ocean, in which day/night OLR differences are very small. Direct comparisons of the $AIRS_{AVG}$ OLR with CERES OLR data sets are therefore most meaningful in those regions.

2.0 The AIRS Version-6 OLR and CERES_EBAF Edition 4.0 OLR Data Sets

2.1 AIRS Version 6-OLR

AIRS is a high spectral resolution infrared (IR) atmospheric sounder flying on the Earth Observing System (EOS) Aqua satellite, alongside CERES and the microwave (MW) sounders AMSU A1/A2. AIRS/AMSU Version 6 uses both AIRS and AMSU radiances in the generation of products. The AIRS/AMSU Version-6 data set, henceforth referred to as AIRS Version 6, began in September 2002 and extends through August 2016, after which AMSU A2 ceased to function. AIRS Version-6 generates Level-2 values of AIRS OLR for each AIRS Field of View (FOV) as a function of the AIRS retrieved geophysical state in that FOV via use of an OLR

Radiative Transfer Algorithm (RTA). AIRS/AMSU Version-6 uses no information other than the AIRS/AMSU radiances in the generation of AIRS retrieved products and OLR, with the exception of a 6 hour forecasted surface pressure, used in the calculations of expected channel radiances as a function of geophysical parameters, as well as in the calculation of AIRS OLR for a geophysical state.

The AIRS Version-6 OLR product has improved considerably compared to that of AIRS Version-5 for two major reasons. The first is that the AIRS Version-6 retrieved geophysical states (Susskind et al., 2014) are more accurate than the AIRS Version-5 geophysical states (Susskind et al., 2011). In addition, the AIRS Version-6 OLR RTA (Iacono et al., 2008) is considerably more accurate than the OLR RTA (Mehta and Susskind 1999a, Mehta and Susskind 1999b) used in Version-5.

We describe the methodology used to compute AIRS OLR in detail in Appendix A. Appendix A shows that values of AIRS OLR in a FOV are linear combinations of OLR_{CLR}, the value of OLR computed for the clear portion of the FOV, and OLR_{CLD}, the OLR computed for different cloudy portions of the FOV. OLR_{CLR} increases with increases in the earth's skin surface temperature T_s, with increases in the earth's surface skin spectral emissivity ε_ν, and with increases in the atmospheric temperature profile $T(p)$. On the other hand, OLR_{CLR} generally decreases with increases in the atmospheric water vapor profile $q(p)$, especially in the mid-upper troposphere. Values of OLR_{CLR} also depend on the vertical distributions of trace gases such as O_3, CH_4, CO_2, and CO. OLR_{CLD} depends on these same geophysical parameters, and also strongly depends on the heights, amounts, and spectral

emissivities of multiple layers of cloud cover as seen from above in the FOV, especially those of high clouds. Appendix A explains why AIRS Version-6 determines only the product of the fractional cloudiness α as seen from above in different FOVs, and ε the cloud emissivity. We call this product $\alpha\varepsilon$ the "Radiative Effective Cloud Fraction".

AIRS Version-6 generates single FOV Level-2 (L2) values of OLR under all cloud conditions in which the cloud parameter retrieval in that FOV has converged. This convergence occurs close to 100% of the time. All generated L2 values of AIRS OLR are included in the AIRS gridded Level-3 (L3) OLR product.

The methodology used to compute AIRS OLR involves a sum of separate calculations performed in each of 16 spectral bands. Table A1 in the Appendix shows that almost half of OLR originates from bands with frequencies lower than 650 cm^{-1}, the lowest frequency observed by AIRS. Table A1 also shows that LW flux at these lower frequencies is relatively insensitive to cloud characteristics because, on the average, the presence of clouds decreases OLR by a total of only 4.8 W/m^2 over those frequencies not observed by AIRS. We obtained the AIRS Version-6 data set from the Goddard Earth Sciences (GES) Data and Information Services Center (DISC) doi:10.5067/Aqua/AIRS/DATA319.

2.2 CERES EBAF Edition 4.0 OLR

The CERES_EBAF Edition 4.0 data set began in March 2000 and, at the time of this writing, extends through November 2019. CERES instruments fly on EOS Terra in a sun-synchronous orbit with a descending mode equator crossing time of 10:30 AM local time, as well as on EOS Aqua, alongside AIRS, in a sun-synchronous orbit with an ascending mode equator crossing time of 1:30 PM local time. Each CERES instrument measures filtered radiances in three distinct bands: the shortwave band (SW), with wavelengths between 0.3 and 5 μm; the total band (TOT), with wavelengths between 0.3 and 200 μm; and the window band (WN), with wavelengths between 8 and 12 μm. Unfiltered SW, LW, and WN radiances are determined following Loeb et al. (2001). CERES LW radiances are determined by subtracting the CERES SW band radiances from the CERES TOT radiances. The CERES-EBAF Edition 4.0 OLR product utilizes the CERES SYN 1deg Ed-4.0 LW data product that combines observations from CERES instruments on each of the Terra and Aqua satellites with geostationary imager measurements (Doelling et al., 2013) in order to provide TOA fluxes hourly in 1°x1° latitude-longitude regions.

The CERES_EBAF Edition 4.0 data set utilizes an objective constrainment algorithm described in Loeb et al. (2018). This approach makes a one-time adjustment to SW and LW TOA fluxes, within their ranges of uncertainty, to remove inconsistencies between the 10-year (July 2005-June 2015) average CERES all-sky global net TOA flux and heat storage in the Earth-atmosphere system based on findings using in-situ data. We obtained the CERES EBAF_Edition 4.0 OLR data set from https://ceres.larc.nasa.gov/products-info.php?product=EBAF.

3.0 Inter-comparison of AIRS and CERES OLR Data Records

This section compares monthly mean values of fourteen years of the three AIRS Version 6 OLR data sets and the CERES_EBAF Edition 4.0 OLR data set with each other on a number of different spatial domains: global; the Northern Hemisphere extra-tropics (NHET) 90°N-30°N; the tropics 30°N-30°S; and the Southern Hemisphere extra-tropics (SHET) 30°S-90°S. The tropics represent 50% of the area of the earth, and the NHET and SHET each represent 25% of the earth's area.

Figures 1a-1d show Version-6 monthly mean values, starting from the beginning of the AIRS data set September 2002, of $AIRS_{PM}$ OLR, $AIRS_{AM}$ OLR, $AIRS_{AVG}$ OLR, and CERES_EBAF Edition 4.0 OLR in four spatial domains. The vertical black lines mark results for each January, and the numbers indicate the calendar year between each January. Figure 1a shows results for global mean values of OLR. All global mean OLR data sets contain a large seasonal cycle as well as a pronounced diurnal signal. AIRS global mean OLR is greater at roughly 1:30 PM local time (pink) than it is at roughly 1:30 AM (red). This is because, everything else being equal, OLR increases with increasing surface and atmospheric temperatures, both of which tend to be largest in the afternoon. In the global mean sense, $AIRS_{AM}$ OLR matches CERES OLR almost perfectly, while $AIRS_{PM}$ OLR is larger than CERES OLR. We later show this finding to be the result of cancellation of positive and negative differences between $AIRS_{AM}$ OLR and CERES OLR in different spatial domains. $AIRS_{AVG}$ OLR values (blue) lie between those of $AIRS_{AM}$ and those of $AIRS_{PM}$.

225 Figures 1b-d show analogous results for tropical mean OLR, NHET mean OLR, and
226 SHET mean OLR respectively. AIRS and CERES tropical mean OLR time series show
227 similar relative differences compared to those of global mean OLR. $AIRS_{AM}$ tropical
228 mean OLR again matches that of CERES almost perfectly, and $AIRS_{PM}$ tropical mean
229 OLR is larger than CERES tropical mean OLR. Tropical mean OLR has a seasonal
230 variability, with minima in January and maxima in July, but with a significantly
231 smaller and more complex seasonal cycle than that of global mean OLR. NHET and
232 SHET area mean OLR time series each show pronounced out of phase seasonal
233 cycles having maxima in local summer and minima in local winter. The NHET OLR
234 seasonal cycle is larger than that of the SHET. Consequently, the global mean OLR
235 seasonal cycle is in phase with, but smaller than, that of NHET.

236 The time of day dependences of the NHET and SHET AIRS OLR time series are more
237 complex than those of either global mean OLR or tropical mean OLR, as are the
238 relationships between AIRS OLR and CERES OLR. The amplitudes of OLR diurnal
239 differences are considerably larger in the NHET, which is predominantly land, than
240 they are in the SHET, which is predominantly ocean. This phenomenon occurs
241 because oceanic surface skin temperatures have both smaller seasonal cycles and
242 smaller diurnal cycles than those for land.

243 Figures 2a-d present the differences (AIRS minus CERES) between the AIRS and
244 CERES monthly mean area mean OLR values shown in Figures 1a-d. Global mean
245 values of $AIRS_{AM}$ OLR match those of CERES OLR extremely closely in every month of
246 the time-period under study. Global mean values of $AIRS_{PM}$ OLR exceed those of

CERES OLR by about 7W/m^2. This bias has a small seasonal cycle, with minima in Northern Hemisphere winter. The tropics contain similar, but somewhat larger, differences between the time of day dependent AIRS OLR data sets and the CERES OLR data set.

Levels of agreement between monthly mean values of AIRS OLR and CERES OLR show different characteristics in the extra-tropics however. Figure 2c shows a roughly out of phase NHET relationship of the seasonal cycle differences between $AIRS_{PM}$ OLR and CERES OLR on the one hand (pink), and between $AIRS_{AM}$ OLR and CERES OLR on the other hand (red). NHET $AIRS_{AM}$ area mean values of OLR match those of CERES OLR almost perfectly during local winter, but are slightly negative compared to CERES OLR during local spring/summer when the positive biases between $AIRS_{PM}$ OLR and CERES OLR are largest. In the SHET, $AIRS_{AM}$ OLR matches CERES OLR almost perfectly in local spring/summer, but is larger than CERES OLR during local fall/winter. A consequence of the hemispheric asymmetries in the $AIRS_{AM}$ and $AIRS_{PM}$ OLR differences from CERES OLR is that the $AIRS_{AVG}$ OLR time series has only very small seasonal cycle differences from that of CERES OLR in each extra-tropical region.

Table 1 shows the biases between monthly mean values of AIRS OLR and CERES OLR for each spatial domain, as well as their temporal standard deviations (STDs). Table 1 also includes the slopes of the linear least squares fits to the differences between AIRS OLR and CERES OLR (W/m^2/yr), along with their uncertainties, which represent twice the STDs of the linear least squares fits to the time series. The

biases between area-mean values of $AIRS_{AM}$ OLR and CERES OLR are smallest in all spatial regions. Area mean biases do not tell the whole story, however. The temporal STDs of the time series differences between AIRS OLR and CERES OLR are in general smallest for $AIRS_{AVG}$ OLR, especially in the extra-tropics, with values varying from 0.25 W/m^2 to 0.37 W/m^2 in all regions. This indicates that up to a bias, the $AIRS_{AVG}$ OLR and CERES OLR time series agree best over all seasons and over time. The differences between the $AIRS_{AVG}$ OLR time series and that of CERES OLR have at most very small drifts in time in all spatial domains.

3.1 Inter-comparison of AIRS OLR and CERES OLR Monthly Climatologies

We generated climatologies for $AIRS_{AM}$ OLR, $AIRS_{PM}$ OLR, and CERES OLR for each month of the year, on a 1°x1° spatial scale, by taking the monthly mean averages of OLR in that grid box over the fourteen-year period under study. We generated $AIRS_{AVG}$ OLR climatologies by first taking the average of the monthly mean $AIRS_{PM}$ and $AIRS_{AM}$ OLR products for each month and subsequently producing analogous $AIRS_{AVG}$ climatologies for that month.

Figures 3a and 3b show the spatial distributions of the January $AIRS_{AVG}$ OLR climatology and of the January CERES OLR climatology respectively. The statistics on each figure indicate the area weighted global mean value of each field as well as its area weighted spatial STD. January climatological OLR values are very low at high latitudes where surface skin temperatures and atmospheric temperatures are both low. Very low OLR climatological values also occur in some tropical areas that contain large amounts of high clouds resulting from significant convective activity in

these regions. Such areas also tend to contain large amounts of Mid-Upper Tropospheric Humidity (MUTH), which, like high cloud cover, also lowers OLR, though to a lesser extent. Figures 3c-e show respectively the spatial differences from the January CERES OLR climatology of the January $AIRS_{AVG}$, $AIRS_{AM}$, and $AIRS_{PM}$ OLR climatologies from the January CERES OLR climatology, and Figure 3f shows the differences between the January $AIRS_{PM}$ OLR climatology and the January $AIRS_{AM}$ OLR climatology.

While January climatological values of $AIRS_{AM}$ OLR best match those of CERES OLR in the global mean sense, the global mean match between values of $AIRS_{AM}$ OLR and CERES OLR is very misleading. The January $AIRS_{AM}$ OLR climatology is somewhat higher than that of CERES OLR over ocean, but is significantly lower than that of CERES OLR over arid land, which cools considerably at night, with an area weighted spatial STD of 4.19 W/m^2. Figure 3c shows that the spatial differences between the January $AIRS_{AVG}$ OLR climatology and the January CERES OLR climatology are much more homogeneous, with a spatial STD of 2.58 W/m^2. This result also demonstrates that the AIRS OLR calculations treat the large effects of tropical clouds on OLR very accurately.

The biggest differences between the January $AIRS_{AVG}$ OLR climatology and the January CERES OLR climatology occur in areas in which the differences between the January $AIRS_{PM}$ and $AIRS_{AM}$ OLR climatologies are largest, as shown in Figure3f. AIRS and CERES temporal sampling differences are therefore a factor affecting the spatial differences between the January $AIRS_{AVG}$ OLR and CERES OLR climatologies.

313 AIRS diurnal January OLR climatological differences are greater than 45 W/m^2 over
314 arid regions such as the Sahara Desert, the southern parts of South America and
315 South Africa, and Western Australia. The AIRS January OLR climatology in some
316 Southern Hemisphere tropical oceanic areas is actually somewhat lower at 1:30 PM
317 than it is at 1:30 AM. This is a result of increases in low cloud cover in these areas as
318 sampled by Aqua at 1:30 AM as compared to 1:30 PM.

319 Doelling et al. (2013) addressed ways to account for diurnal variability of OLR in a
320 CERES OLR product. His CERES GEO-combined method, used in CERES_EBAF
321 Edition 4.0, incorporates hourly imager data from five geostationary satellites to
322 help account for changes in OLR between CERES observation times. Harries et al.
323 (2005) obtained very good results using the CERES GEO-combined method, after
324 removing calibration differences for each CERES instrument, when compared to 15-
325 min resolution OLR as observed from Geostationary Earth Radiation Budget (GERB).

326 Using data for January 2005, Doelling et al. (2013) showed that the amplitude of the
327 OLR diurnal cycle can reach 35 W/m^2 over a Saharan desert location (30.5°N, 0.5°E),
328 over 8 W/m^2 in a marine stratus location (20.5°S, 10.5°E), and over 45 W/m^2 in a
329 land convective region (20.5°S, 20.5°E).

330 Figures 4a-f show analogous July OLR climatologies and climatological differences.
331 AIRS OLR diurnal differences in arid areas are in general larger in July than they are
332 in January in both hemispheres. As in January, the differences of $AIRS_{AVG}$ OLR from
333 CERES OLR are for the most part spatially homogeneous with the exception of land
334 areas containing very large diurnal differences of OLR.

4.0 Factors Contributing to Diurnal OLR Climatological Differences

Figures 3f and 4f depict diurnal differences of the AIRS January OLR climatology and of the July OLR climatology, respectively. Positive OLR diurnal differences are greatest over arid land in both seasons, with values that are largest in the tropics and during local summer in the extra-tropics. Moderately positive diurnal OLR differences also occur over elevated terrain in polar summer in Eastern Antarctica (January) and over Greenland (July). Polar OLR diurnal differences are close to zero in both months in local winter. Figure 5 shows diurnal climatological differences of three AIRS derived geophysical parameters for January and July on which OLR strongly depends: surface skin temperature T_s; Radiative Effective Cloud Fraction $\alpha\varepsilon$; and 500 mb specific humidity *q(500)*. OLR increases with increases in T_s and decreases with increases in $\alpha\varepsilon$ and with increases in *q(500)*. For this reason, positive (negative) values of diurnal differences of T_s are shown in Figure 5 in shades of red and green (blue and yellow), and the reverse color code is used for diurnal differences of $\alpha\varepsilon$ and *q(500)*. Diurnal differences of T_s are always positive and are largest over tropical and mid-latitude land, especially in local summer. Moderately positive T_s diurnal differences also occur in polar summer over elevated terrain such as Eastern Antarctica and Greenland. Analogous features appear in the diurnal OLR differences shown in Figures 3f and 4f over land. This demonstrates that diurnal T_s differences affect those of OLR in these regions. Diurnal T_s differences are very small over ocean. Diurnal OLR differences over ocean result primarily from diurnal $\alpha\varepsilon$ sampling differences

Over land, regions containing large positive diurnal T_s differences (red) often contain large negative diurnal $\alpha\varepsilon$ differences (red). Reduction of cloud cover during the day in these regions further enhances the positive temporal effect on OLR of afternoon warming of land temperatures. One might think that afternoon values of $\alpha\varepsilon$ over hot convective regions would be high because of increased afternoon thunderstorm activity, but this phenomenon usually occurs closer to 3:30 PM local time, a time AIRS does not observe. Diurnal OLR differences over some convective regions are reduced to some extent by diurnal changes of opposite sign of *q(500)*.

5.0 Inter-comparison of AIRS OLR and CERES OLR Anomaly Time Series

Figure 6 shows anomaly time series of AIRS OLR and CERES OLR as a function of time over the period September 2002 through August 2016. Figure 6a shows global mean anomalies, Figure 6b shows tropical mean OLR anomalies, and Figures 6c and 6d show NHET and SHET OLR anomalies respectively. Diurnal differences between AIRS OLR anomalies exist, but they are small compared to the anomalies themselves.

Figure 6b includes values of the ENI. Tropical mean OLR anomalies tend to track the ENI to some extent. The positive tropical mean OLR anomalies in early 2003, in 2007, in early 2010, in 2015, and in early 2016, generally correspond to periods with positive values of the ENI, during which there are positive T_s anomalies in the combined Niño-3 and Niño-4 regions. This is especially true in 2015 and 2016. The negative tropical OLR anomalies in 2006, in 2007, in 2008, and in mid-2010 to early 2012, generally correspond to periods with negative values of the ENI, during which there are negative T_s anomalies in the combined Niño-3 and Niño-4 regions. Figure

379 6b indicates that tropical mean OLR anomalies tend to lag the ENI by a small amount
380 in time. The unlagged temporal correlation of tropical mean OLR anomalies with the
381 ENI is 0.55. The temporal correlation of tropical mean OLR anomalies with the ENI
382 is largest after a lag of OLR by two months from the ENI, with a lagged temporal
383 correlation of 0.64. Global mean OLR anomalies also track the ENI to some extent
384 because the tropics constitute 50% of the globe.

385 NHET OLR anomalies contain a substantial positive peak in early 2016, as do
386 tropical mean and global mean OLR anomalies. Such positive anomalies in early
387 2016 do not occur in the SHET OLR anomaly time series.

388 5.1 Comparison of ARCs of AIRS OLR and CERES OLR

389 Table 2 presents area mean ARC's ($W/m^2/yr$) of all AIRS OLR anomaly time series,
390 as well as those of CERES OLR. ARCs of all AIRS OLR anomaly time series show
391 excellent agreement with those of CERES in all regions. This indicates that there was
392 essentially no drift between the AIRS and CERES OLR data sets over the 14-year
393 time period studied.

394 Global mean OLR ARCs are all very slightly positive, with values that are within their
395 uncertainties. Tropical mean OLR ARCs are all slightly negative, again with values
396 within their uncertainties. SHET OLR ARCs are all essentially zero. On the other
397 hand, NHET OLR ARCs are all very positive over this time-period and have values
398 considerably larger than their uncertainties. This finding is the result of the large
399 NHET positive OLR anomalies that occurred in early 2016. The existence of the

small positive global mean value of OLR ARCs arises primarily from those in the NHET, which represents 25% of the area of the globe.

With the exception of the SHET, which contains little land, $AIRS_{PM}$ OLR ARCs are all more negative, or less positive, than $AIRS_{AM}$ OLR ARCs. While the area mean differences between $AIRS_{PM}$ and $AIRS_{AM}$ OLR ARCs are within their uncertainties, these differences are not a result of random noise and are a physical result discussed later.

ARCs of any geophysical parameter can be time-period dependent. Su et al. (2017) analyzed AIRS data through December 2013 and showed a significant negative tropical mean OLR trend of approximately -1.0 W/m^2/decade. The negative short-term OLR trend Su et al. (2017) observed was a result of the 2013 La Niña event that took place near the end of the time-period they studied.

5.2 Spatial Distributions of ARCs and ENCs of AIRS and CERES OLR

Figures 7a and 7b show the spatial distributions on a 1˚ latitude by 1˚ longitude grid of the ARCs of $AIRS_{AVG}$ OLR and CERES OLR. All grid point values shown in these and subsequent spatial plots have a three-point smoother applied to them in both the latitude and longitude domains. Reds and greens show positive OLR ARCs and blues and yellows show negative OLR ARCs. At least as significant as the values of the OLR ARCs shown in Figures 7a and 7b are their very coherent spatial structures, which are virtually indistinguishable from each other. These figures, and all subsequent spatial plots, contain a black box surrounding the NOAA Niño-4 region and a gray box surrounding the NOAA Niño-3 region.

While all global mean and tropical mean OLR ARCs are essentially zero within their uncertainties, there is considerable spatially coherent structure in the ARCs of OLR, especially in the tropics. In particular, there are large negative OLR ARCs surrounding the equator in the region 160˚W eastward to 70˚W, indicating that OLR has decreased in this region over the time-period under study. Smaller, but significant, positive OLR ARCs exist in equatorial areas westward and eastward of this region that compensate for those negative values in the tropical mean sense.

Figure 7c shows the spatial differences between the ARCs of $AIRS_{AVG}$ OLR and those of CERES OLR. The area weighted spatial correlation between the two sets of OLR ARCs is 0.978, and the spatial STD of their differences is 0.047 $W/m^2/yr$. $AIRS_{AVG}$ OLR ARCs tend to be slightly more positive (or less negative) than those of CERES over tropical oceans, and more negative (or less positive) than those of CERES over the Sahara Desert, Saudi Arabia, and Australia. The area weighted global mean ARC of $AIRS_{AVG}$ OLR for this period is 0.005 $W/m^2/yr$ less positive than that of CERES.

Figure 7d shows the spatial differences between the ARCs of $AIRS_{PM}$ OLR and those of $AIRS_{AM}$ OLR. The largest diurnal differences of ARCs of AIRS OLR occur over Australia. Therefore, temporal sampling differences may be a factor affecting the small differences between the ARCs of $AIRS_{AVG}$ OLR and those of CERES OLR over Australia. Unlike over land, diurnal differences of $AIRS_{AVG}$ OLR ARCs are scattered over ocean. This is primarily the result of sampling differences of cloud cover as observed separately during the ascending and the descending orbits of Aqua.

443 Figures 7e and 7f show patterns of the ENCs of the $AIRS_{AVG}$ OLR and of the CERES
444 OLR anomaly time series. ENCs represent correlations and are therefore unit-less,
445 with values ranging from -1.0 to 1.0. Reds and greens indicate spatial regions with
446 positive ENCs, in which anomalies at a given time tend to be of the same sign as the
447 ENI, while blues and yellows indicate regions with negative ENCs in which the
448 reverse is true. As with ARCs, there is excellent agreement between the spatial
449 patterns of the ENCs of $AIRS_{AVG}$ OLR and the ENCs of CERES OLR. OLR ENCs can be
450 very large in the tropics, especially within the Niño-4 region in which they are very
451 negative. This indicates that OLR typically has negative anomalies within the Niño-4
452 region during El Niño conditions and positive anomalies within the Niño-4 region
453 during La Niña conditions.

454 While there are similarities between the patterns of ARCs and ENCs of OLR in the
455 tropics, there are also some significant differences between them. Unlike OLR ARCs,
456 which have both positive and negative values within the Niño-4 region, ENCs of OLR
457 have large negative values within the entire Niño-4 region. In addition, ENCs of OLR
458 are small and have mixed signs within the Niño-3 region while ARCs of OLR are
459 large and negative within in this region.

460 The differences in signs and relative magnitudes in the tropics with regard to ARCs
461 of OLR on the one hand, and ENCs of OLR on the other hand, are a result of when
462 and where El Niño/La Niña activity took place during the period under study. As will
463 be shown later, most El Niño/La Niña activity took place within the Niño-4 region,
464 and it occurred primarily in the early to middle part of the time-period under study.

Consequently, the large negative OLR ENCs found within the Niño-4 region do not occur within the Niño-3 region.

In the absence of other changes, OLR increases with increasing T_s, which, by definition, has a positive correlation with the ENI within the Niño-4 region. Therefore, one might expect to have positive OLR ENCs within the Niño-4 region. The effect of local increases (decreases) of T_s on OLR within the Niño-4 region at a given time is more than offset by corresponding local increases (decreases) in both high cloud cover and MUTH, each of which decreases (increases) OLR. Areas surrounding Niño-4 to the north and south have positive OLR ENCs. This indicates that convective activity in those areas tended to increase (decrease) during periods when it decreased (increased) within the Niño-4 region.

6.0 ARCs and ENCs of Important Geophysical Parameters Affecting OLR

Computed values of AIRS OLR in a FOV depend on the AIRS retrieved geophysical state in that FOV. Therefore, one can attribute ARCs and ENCs of AIRS OLR to those of the AIRS retrieved surface and atmospheric geophysical parameters. It is impractical to discuss relevant results of all the geophysical parameters affecting OLR. In this paper, for demonstrative purposes, we concentrate on surface skin temperature T_s; surface air temperature T_{sa}; 500 mb specific humidity *q(500)*; and Radiative Effective Cloud Fraction $\alpha\varepsilon$. Figure 8a shows the spatial distribution of ARCs of $AIRS_{AVG}$ T_s. The color code in Figure 8a is analogous to that used in Figure 7a, with positive values depicted in reds and greens and negative values depicted in blues and yellows. In the global mean sense, T_s warmed at a rate of 0.019K/yr over

487 the 14-year time period under study. While this increase is consistent with "global
488 warming", the earth has not warmed uniformly over the time-period under study.
489 The earth's surface has warmed considerably poleward of 70°N, especially west of
490 the dateline, as well as in an area centered at 50°N and 40°E. There has also been
491 slight warming during this period over some tropical oceanic areas, especially
492 within the Niño-3 region. On the other hand, there has been considerable cooling
493 during this period over Greenland and the ocean surrounding it, as well as over
494 Eastern Australia and over some oceanic areas poleward of 60°S.

495 OLR increases with increasing $T_{s,}$ everything else being equal. Consequently,
496 features of ARCs of T_s will look like those of ARCs of OLR to the extent that changes
497 in T_s are the driving force behind changes in OLR. Features of T_s ARCs in mid-high
498 latitudes are readily apparent in those of OLR ARCs. Therefore, changes in OLR over
499 time in these regions resulted primarily from changes in T_s. Note, in particular, the
500 in-phase relationship poleward of 60°N between the ARCs of OLR and the ARCs of T_s.

501 Figure 8b shows ARCs of T_{sa} using the same color scale as in Figure 8a. While OLR
502 depends significantly on T_s, it depends very little on T_{sa}. Nevertheless, we show T_{sa}
503 because surface air temperature represents the environment in which we live. ARCs
504 of T_{sa} are very similar to those of T_s, but are somewhat smaller and are smoother in
505 space. Globally, surface air temperature warmed at a rate of 0.16K/yr, which is
506 slightly less than that of surface skin temperature.

507 Figures 8c and 8d show ARCs of *q(500)* and ARCs of $\alpha\varepsilon$ respectively. Global mean
508 ARCs of *q(500)* and $\alpha\varepsilon$ are each positive. This indicates that AIRS shows that the

509 Earth has both moistened in the middle troposphere during the time-period under
510 study and has gotten somewhat cloudier over this time-period as well. A
511 comparison of Figures 7a and 8c demonstrates that the spatial distribution of
512 tropical ARCs of *q(500)* is virtually identical to that of OLR, albeit with an opposite
513 sign. This shows that temporal changes in tropical OLR are closely related to those
514 of *q(500)*. The spatial agreement between ARCs of OLR with ARCs of $\alpha\varepsilon$ is not as
515 good as it is with ARCs of *q(500)* because cloud fraction, as shown, refers to total
516 cloud cover, independent of cloud top pressure. ARCs of $\alpha\varepsilon$ for high clouds (not
517 shown) gives a closer spatial agreement with ARCs of OLR.

518 Figures 9a-d show the spatial distributions of ENCs of $AIRS_{AVG}$ T_s, T_{sa}, *q(500)*, and $\alpha\varepsilon$
519 respectively. Figure 9a shows that the largest correlations of T_s with the ENI occur in
520 the tropics. As expected, T_s anomalies have large positive correlations with the ENI
521 over each of the Niño-4 and Niño-3 regions. Figure 9a shows that T_s anomalies also
522 have positive correlations with the ENI, though less so, in areas immediately to the
523 north and south of the Niño-4 and Niño-3 regions, and that these areas containing
524 positive T_s correlations with the ENI extend to the west coasts of the United States
525 and Canada. Regions to their north, south, and west contain significant negative
526 correlations of T_s with the ENI. The spatial distributions of ENCs of T_s and ENCs of
527 T_{sa} are very similar to each other, but the magnitudes of ENCs of T_s are somewhat
528 larger than the magnitudes of ENCs of T_{sa}.

529 In the tropics, spatial patterns of ENCs of *q(500)* are similar to those of ENCs of T_s
530 and ENCs of T_{sa} because periods of locally warmer (cooler) surface temperatures

tend to correspond to periods of locally moister (drier) mid-tropospheres. Tropical OLR ENCs, shown in Figure 7c, are for the most part anti-correlated with ENCs of *q(500)* because local increases in *q(500)* result in local decreases in OLR. Tropical ENCs of $\alpha\varepsilon$ show some similarity to those of *q(500)* but with significant differences, particularly within the Niño-3 region and also off the west coast of North America.

7.0 Hovmöller Diagrams

Hovmöller diagrams are plots of anomalies of geophysical parameters integrated over a range of latitudes as a function of time and longitude. Figure 7e shows that the largest correlations and anti-correlations of OLR with the ENI occur near the equator, in a region extending from 100°E longitude eastward to 80°W longitude. Hovmöller diagrams help explain the factors affecting this feature. Figures 10a-10d show monthly mean Hovmöller Diagrams of T_s, OLR, 500 mb specific humidity, and $\alpha\varepsilon$ integrated over the latitude range 5°N through 5°S (vertical scale) in each 1˚ longitude bin (horizontal scale) for the time-period September 2002 through August 2016. We applied a 5 point (5 month) linear smoothing in the vertical and a 15-point (15 degree) linear smoothing in the horizontal in order to minimize the effects of small discontinuities between adjacent rectangular grid points on the figures. Most of the Hovmöller domain is ocean. There are three relatively small land areas near the equator: South America, Africa, and Indonesia. These land areas each lie between the three sets of black vertical lines indicated in Figures 10a-10d. The three adjacent vertical gray lines in Figure 10 indicate the longitudinal extents of the Niño-4 region and Niño-3 region respectively.

553 Figure 10a depicts positive T_s anomalies in shades of red and yellow, and negative T_s
554 anomalies in shades of blue and purple. The largest equatorial T_s anomalies
555 occurred over the ocean between 160˚E, the western edge of the Niño-4 region, and
556 90˚W, the eastern edge of the Niño-3 region, and sometimes extended further
557 eastward to 80˚W off the west coast of South America. Significant El Niño events
558 (dark red and yellow) occurred within the Niño-4 region in 2003, 2010, 2015, and
559 2016, and significant La Niña events (dark blue and purple) occurred within the
560 Niño-4 region in 2008 and 2011. The El Niño event beginning in mid-2015 differs in
561 location from the earlier El Niño events in that it occurred primarily within the
562 Niño-3 region and extended to the west coast of South America.

563 Figure 10b depicts the Hovmöller diagram of OLR. Figure 10b demonstrates that
564 equatorial OLR anomalies are highly anti-correlated with T_s anomalies within the
565 Niño-4 region. The same result occurs within the Niño-3 region to some extent after
566 mid-2015. Figures 10a and 10b explain why OLR anomalies within the Niño-4
567 region are highly anti-correlated with the ENI. ENCs of OLR within the Niño-3 region
568 are smaller than they are within the Niño-4 region, and can be positive or negative,
569 because OLR anomalies within the Niño-3 region have a lower correlation with the
570 ENI in the early part of the time-period, during which T_s anomalies occurred
571 primarily within the Niño-4 region.

572 Figures 10c and 10d show analogous Hovmöller diagrams of *q(500)* and $\alpha\varepsilon$
573 respectively. Anomaly patterns of *q(500)* within the Niño-3 and Niño-4 regions
574 generally follow those of T_s very closely, both in relative magnitudes and phase. This

demonstrates that positive (negative) SST anomalies correspond to periods of locally increased (decreased) convection, which in turn lead to enhancement (suppression) of *q(500)*. These periods often correspond to periods of increased (decreased) high cloud cover (not shown). Local values of OLR therefore decrease (increase) during El Niño (La Niña) periods. Cloud cover as shown includes amounts of low clouds. Such clouds are not associated convective activity.

8.0 Diurnal Differences of ARCs and ENCs of Relevant Geophysical Parameters

This section compares diurnal differences of the ARCs and ENCs of AIRS OLR with those of select geophysical parameters on which OLR depends. Figures 11a-c show the spatial distributions of the ARCs of $AIRS_{PM}$ T_s, of the ARCs of $AIRS_{AM}$ T_s, and of the difference between their ARCs ($AIRS_{PM}$ minus $AIRS_{AM}$) respectively. The spatial features of the PM/AM differences of OLR ARCs, shown in Figure 7d, tend to match those of Figure 11c in both signs and relative magnitudes in places over land where both sets of diurnal differences are large. This shows that over land, diurnal differences of ARCs of T_s are a significant factor affecting the diurnal differences of ARCs of OLR. Figure 11d shows the diurnal differences of ARCs of *q(500)*, which contain only small-scale features that occur primarily over ocean. These features are most likely a result of sampling differences of anomalies over the month as observed by AIRS at 1:30 PM and at 1:30 AM respectively.

Figures 12a-d are analogous to Figures 11a-d, but with regard to ENCs of the same geophysical parameters. ENCs of T_s at 1:30 PM are very positive over Australia in those regions in which 1:30 PM ARCs of T_s are very negative. On the other hand,

ARCs and ENCs of T_s over Australia at 1:30 AM are each small. It is apparent that the large negative diurnal differences of the ARCs of both T_s and of OLR in Australia are the result of positive correlations of T_s with El Niño/La Niña activity that occurred during the day but did not occur appreciably at night. These differences are largest over Eastern Australia, which we define as eastward of 140°E longitude. As with ARCs, diurnal differences of ENCs *q(500)* have only very small spatial scales, related primarily to sampling differences of *q(500)* observed at different times of day.

8.1 Diurnal differences of T_s Anomaly Time Series over Eastern Australia

Figures 13a-13c show monthly mean T_s anomaly time series over Eastern Australia for 1:30 PM, for 1:30 AM, and for 1:30 PM minus 1:30 AM respectively. These figures also contain the ENI multiplied by two. The Eastern Australia PM T_s anomaly time series shows considerable high frequency monthly mean variability not found in the ENI. Nevertheless, there is a coarse in-phase relationship over Eastern Australia between 1:30 PM T_s anomalies and the ENI, with a temporal correlation of 0.45. There are positive PM T_s anomalies in 2002, 2005, late 2006, late 2009, early 2015, and early 2016, which are all in phase with positive values of the ENI. Even more significant are the negative PM T_s anomalies that occurred in late 2007, early 2008, mid-late 2010, and 2011, which are in phase with negative values of the ENI. The negative trend of Eastern Australian PM T_s anomalies observed over the time-period under study is primarily the result of the large negative PM T_s anomalies that occurred during the La Niña period from mid-2010 through late 2011. This implies

618 that daytime surface skin temperatures over Eastern Australia were significantly
619 cooler than normal during this large La Niña event.

620 The AM T_s anomaly time series over Eastern Australia is shown in Figure 13b. AM T_s
621 anomalies are much smaller than PM T_s anomalies, and have a correlation with the
622 ENI of only 0.11. This implies that unlike during the day, El Niño/La Niña events
623 had little effect on nighttime T_s anomalies over Eastern Australia. Figure 13c,
624 showing the difference between the Eastern Australian 1:30 PM and 1:30 AM T_s
625 anomalies, is similar in appearance to Figure 13a because AM T_s anomalies were
626 small as compared to PM T_s anomalies.

627 9.0 Summary

628 This paper compares the temporal and spatial characteristics of three monthly
629 mean L3 AIRS Version-6 OLR data sets $AIRS_{PM}$, $AIRS_{AM}$, and $AIRS_{AVG}$, with those of
630 the L3 CERES_EBAF Edition 4.0 OLR data set over a14-year overlap time-period of
631 the two data sets, September 2002 through August 2016. AIRS and CERES global
632 mean OLR time series both show pronounced annual cycles, with maxima in July
633 and minima in January. $AIRS_{AVG}$ OLR displays a positive bias as compared to CERES
634 OLR of roughly 3.0 W/m^2 with essentially no drift over the 14 years we compared.
635 At least part of the differences between the computed AIRS OLR product and the
636 observed CERES OLR product is a result of limitations in the AIRS OLR RTA, as well
637 as possible biases in the AIRS retrieved geophysical parameters used in the
638 computation of AIRS OLR. In addition, the CERES OLR product also has calibration

639 uncertainties. Temporal sampling differences in the data used by AIRS and CERES
640 contributed to this bias as well.

641 There is excellent agreement between the ARCs and ENCs of the $AIRS_{AVG}$ OLR
642 anomaly time series and the CERES OLR anomaly time series down to the 1˚ x 1˚
643 spatial scale. The excellent agreement in space and time of the two independently
644 derived OLR data sets serves to validate each OLR data set in terms of both absolute
645 values and stability. This agreement also tends to validate the geophysical
646 parameters derived from the AIRS observations used in the computation of AIRS
647 OLR, and consequently, it allows for the explanation of OLR variability in terms of
648 the variability of geophysical parameters.

649 Fourteen year AIRS and CERES global mean OLR ARCs are essentially zero within
650 their stated uncertainties, defined as twice the STDs of the linear least squares fits to
651 their anomaly time-series. Both AIRS and CERES show, on the other hand, that
652 Northern Hemisphere extra-tropical OLR ARCs have positive values which agree
653 well with each other and are both larger than their uncertainties. This finding is the
654 result of the considerable warming that took place during the period under study
655 from the Greenwich Meridian westward toward the dateline poleward of 70°N.

656 The differences between the AIRS and CERES OLR climatologies, as well as between
657 the AIRS and CERES OLR anomaly time series, are each largest in a region in Eastern
658 Australia in which the ARCs and ENCs of $AIRS_{PM}$ T_s differ considerably from those of
659 $AIRS_{AM}$ T_s.

660

661

662 Appendix A

663 Observed AIRS channel radiances in a FOV depend on the surface, atmospheric and
664 cloud conditions within the FOV. To first order, AIRS observations do not
665 distinguish between upwelling radiation passing through the clouds, which depends
666 on the spectral emissivity of the clouds ε, and radiation coming from around the
667 sides of clouds, which depends on fractional cloud cover, α. Consequently, the
668 Version-6 AIRS cloud parameter retrieval algorithm only determines $\alpha\varepsilon$ the product
669 of these geophysical parameters. We refer to $\alpha\varepsilon$ as the Radiative Effective Cloud
670 Fraction.

671 A-1 Methodology used to compute OLR

672 The methodology used to compute AIRS Version-6 OLR is analogous to that used in
673 AIRS Version-5, but with some important differences. As with AIRS Version-5, AIRS
674 Version-6 assumes that an AIRS FOV contains up to two distinct layers of clouds as
675 seen from above, with cloud top pressures p_{c1} and p_{c2}. Consequently, OLR computed
676 in an AIRS FOV is given by the linear combination of the OLR arising from up to
677 three assumed possible scenes found in the FOV: OLR arising from the clear portion
678 of the scene; and OLR arising from each of the up to two cloudy portions of the scene,
679 covered by p_{c1} and p_{c2}

680 $$OLR = (1-\alpha\varepsilon_1-\alpha\varepsilon_2)\, OLR_{CLR} + \alpha\varepsilon_1 OLR_{CLD1} + \alpha\varepsilon_2 OLR_{CLD2} \qquad (A1)$$

As in Version-5 (Mehta and Susskind 1999a, 1999b), OLR in Version-6 is computed as the sum of fluxes in each of m contiguous spectral bands. AIRS Version-6 uses the Iacono et al. (2008) OLR RTA, which computes OLR_{CLR} as the sum of 16 spectral components according to

$$OLR_{CLR} = \pi \sum_{m=1}^{16} \left[\varepsilon_m B(v_m, T_s) \tau_m(p_s) + \int_{\ln p_s}^{\ln \bar{p}} B(v_m, T(p)) \frac{d\tau_m(p)}{d\ln p} d\ln p \right] \quad (A2)$$

in which $B(v, T)$ is the Planck blackbody function evaluated at frequency v and temperature T; v_m is the central frequency of spectral band m; ε_m is the mean surface emissivity in band m; and $\tau_m(p)$ represents the effective band averaged atmospheric transmittance in band m from pressure p to the top of the atmosphere $\bar{p}$. The terms OLR_{CLD1} and OLR_{CLD2} used in Equation A1 are computed analogously to OLR_{CLR}, but with p_s in Equation A2 being replaced by p_{c1} or $p_{c2.}$ The combined use of Equations A1 and A2 makes the implicit assumption that cloud spectral emissivity is independent of frequency.

The OLR RTA used in AIRS Version 6 (Iacono et al., 2008) has two very important upgrades compared to Mehta and Susskind (1999a; 1999b) which is the OLR RTA used in AIRS Version-5. The parameterization used in Iacono et al. (2008) was generated using more up to date line absorption parameters, especially in the very strong water vapor absorption band near 350 cm^{-1}. In addition, the Iacono et al. (2008) OLR RTA accounts for the variability of additional atmospheric constituents such as CO_2, CO, and CH_4 in the OLR calculation, while Mehta and Susskind (1999a, 1999b) assigned fixed mixing ratios of all trace gases except for water vapor and ozone.

703 Table A1 shows the frequency domains of each of the 16 spectral bands used in
704 Equation A2. Table A1 includes the global mean annual mean individual spectral
705 band fluxes (W/m^2) of each spectral band and the percentage contribution of each
706 spectral band to total OLR. Table A1 also includes the spectral contribution of each
707 band to two other important geophysical parameters not previously discussed in
708 this paper, Clear Sky OLR (OLR_{CLR}) and Longwave Cloud Radiative Forcing (LCWRF).
709 LWCRF, the difference between OLR_{CLR} and OLR, represents the effect of clouds on
710 OLR.

711 Almost half of OLR comes from spectral bands 1-3, extending from 100 cm^{-1} to 630
712 cm^{-1}. This is an extensive spectral domain in which AIRS does not make any
713 observations. The largest approximation made in the current methodology used in
714 the computation of AIRS OLR is that cloud spectral emissivity ε is frequency
715 independent. This assumption most likely does not hold at the longer wavelengths
716 of spectral bands 1-3, especially in the presence of cirrus clouds. The sixth column in
717 Table A1 shows that the presence of clouds in a FOV decreases total flux on the
718 average by about 4.8 W/m^2 in the longwave spectral domain not observed by AIRS.
719 The excellent results shown in this paper demonstrates that the approximation of
720 spectrally independent values of $\alpha\varepsilon$ made in the computation of AIRS OLR works
721 extremely well, at least on the average.

722

723

724

725

726 References

727 Barlow, M., M. Wheeler, B. Lyon, and H. Cullen (2005), Modulation of daily
728 precipitation over Southwest Asia by the Madden-Julian Oscillation, Mon. Weather
729 Rev., 133, 3579-3594.

730 Chiodi, A. M., and D. E. Harrison (2010), Characterizing warm-ENSO variability in the
731 equatorial Pacific: An OLR perspective, J. Clim., 23, 2428-2439.

732 Chu, P. S. and J. B. Wang (1997), Recent climate change in the tropical Western
733 Pacific and Indian Ocean regions as detected by outgoing longwave radiation
734 records, J. Clim., 10, 636-646.

735 Chung, E. S., D. Yeomans, and B. J. Soden (2010), An assessment of climate feedback
736 processes using satellite observations of clear-sky OLR, Geophys. Res. Lett., 37, 7.

737 Dessler, A. E., Z. Zhang, and P. Yang (2008), Water-vapor climate feedback inferred
738 from climate fluctuations, 2003-2008, Geophys. Res. Lett., 35, L20704, doi:
739 10.1029/2008GL035333.

740 Dessler, A. E. (2010), A determination of the cloud feedback from climate variations
741 over the past decade, Science, 330, 1523–1527, doi: 10.1126/ science.1192546.

742 Doelling, D. R., N. G. Loeb, D. F. Keyes, M. L. Nordeen, D. Morstad, C. Nguyen, B. A.
743 Wielicki, D. F. Young, and M. Sun, 2013: Geostationary enhanced temporal
744 interpolation for CERES flux products. J. Atmos. Oceanic Technol., 30, 1072-1090.

745 Harries J. E., J. E. Russell, J. A. Hanafin et al. (2005), The Geostationary Earth
746 Radiation Budget Project, **Bull. Of the American Meteo**. **Soc**. Vol: 86, ISSN: 0003-
747 0007.

748 Hartmann, D., and P. Ceppi (2013), Trends in the CERES Data set 2000-2013: The
749 effects of sea ice and jet shifts and comparison to climate models, J. Clim.,
750 doi:10.1175/JCLI-D-13-00411.1.

751 Hoyos, C. and P. J. Webster (2007), The role of intraseasonal oscillation on the
752 nature of monsoon precipitation, J. Clim., 20 (17), 4402-4424.

753 Huang, Y. and V. Ramaswamy (2009), Evolution and trend of the outgoing long-
754 wave radiation spectrum, J. Clim., 22, 4637–4651, doi:10.1175/2009JCLI2874.1.

755 Iacono, M., J. S. Delamere, E. J. Mlawer, M. W. Shephard, S. A. Clough, and W. D. Collins
756 (2008), Radiative forcing by long-lived greenhouse gases: Calculations with the AER
757 radiative transfer models, J. Geophys. Res., 113, D13103,
758 doi:10.2019/2008JD009944.

759 Jones,C., L.M.V. Carvalho, R.W. Higgins, D.E. Wallisor, and J.K.E. Schemm (2004),
760 Climatology of tropical intraseasonal convective anomalies: 1970-2002, J. Clim, 17,
761 523-539.

762 Kidson, J. W., M. J. Revell, B. Bhaskaran, A. B. Mullan, and J. A. Renwick (2002),
763 Convection patterns in the Tropical Pacific and their influence on the atmospheric
764 circulation at higher latitudes, J. Climate, 15, 137-159.

765 Kiladis, G. N., K. H. Straub, and P. T. Haertel (2005), Zonal and vertical structure of
766 the Madden-Julian Oscillation, J. Atmos. Sci., 62, 2790-2809.

767 Loeb, N. G., K. J. Priestley, D. P. Kratz, E. B. Geier, R. N. Green, B. A. Wielicki, P.O.R.
768 Hinton, S. K. Nolan (2001), Determination of unfiltered radiances from the clouds
769 and the earth's radiant energy system (CERES) instrument, J. Appl. Meteorol., 40,
770 822-835.

771 Loeb N. G., B. A. Wielicki, D. R. Doelling, G. L. Smith, D. F. Keyes, S. Kato, N. Manalo-
772 Smith, T. Wong (2009), Toward optimal closure of the Earth's top-of-atmosphere
773 radiation budget, J. Clim., 22, 748–766.

774 Loeb, N. G., J. M. Lyman, G. C. Johnson, R. P. Allan, D. R. Doelling, T. Wong, B. J. Soden,
775 and G. L. Stephens (2012), Observed changes in top-of-the-atmosphere radiation
776 and upper-ocean heating consistent within uncertainty, Nat. Geosci., 5,
777 doi:10.1038/NGEO1375.

778 Loeb, N. G., N. Manalo-Smith, W. Su, M. Shankar, and S. Thomas (2016), CERES top-
779 of-atmosphere Earth Radiation Budget Climate Data Record: accounting for in-orbit
780 changes in instrument calibration. Remote Sensing, 8(3), 182.
781 http://dx.doi.org/10.3390/rs8030182.

782 Loeb, N. G., D. R. Doelling, H.Wang , W. Su, C. Nguyen, J. G. Corbett, L. Liang, C.
783 Mitrescu, F. G. Rose, and S. Kato (2018), Clouds and the Earth's Radiant Energy

784 System (CERES) Energy Balanced and Filled (EBAF) Top-of-Atmosphere (TOA)
785 Edition-4.0 Data Product. J. Climate, 31, 895-918, doi: 10.1175/JCLI-D-17-0208.1.

786 Mehta, A. V. and J. Susskind (1999a), Outgoing longwave radiation from the TOVS
787 Pathfinder Path A Data Set, J. Geophys. Res., 104, 12193-12212.

788 Mehta, A. V. and J. Susskind (1999b), Longwave radiative flux calculations in the
789 TOVS Pathfinder Path A Data Set, NASA Tech. Rep., GSFC/CR-1999-208643.

790 Soden, B. J. and I. M. Held (2006), An assessment of climate feedbacks in coupled
791 ocean–atmosphere models, J. Clim., 19, 3354-3360.

792 Soden, B. J., I. M. Held, R. Colman, K. M. Shell, J. F. Kiehl, C. A. Shields (2008),
793 Quantifying climate feedbacks using radiative kernels, J. Clim., 21, 3504-3520.

794 Su, W. N.G.Loeb, L.Liang, N.Liu, and C. Liu (2017), The El Niño-Southern Oscillation
795 effect on tropical outgoing longwave radiation: A daytime versus nighttime perspective, J.
796 Geophys. Res. Atmos, 22, 7820–7833, doi: 10.1002/JD0270u 7820–7833.

797 Susskind, J., J. M. Blaisdell, L. Iredell, and F. Keita (2011), Improved temperature
798 sounding and quality control methodology using AIRS/AMSU Data: The AIRS
799 Science Team Version 5 retrieval algorithm. Geoscience and Remote Sensing, IEEE
800 Trans. on Geosci. and Remote Sens., Issue: 99, doi:10.1109/TGRS.2010.2070508, 1-
801 25.

802 Susskind, J., G. Molnar, L. Iredell, and N. G. Loeb (2012), Interannual variability of
803 outgoing longwave radiation as observed by AIRS and CERES, J. Geophys. Res., 117,
804 D23107, doi: 10.1029/2012JD017997.

805 Susskind, J., J. M. Blaisdell, and L. Iredell (2014), Improved methodology for surface
806 and atmospheric soundings, error estimates, and quality control procedures: the
807 atmospheric infrared sounder science team version-6 retrieval algorithm, J. Appl.
808 Rem. Sens., 8, 084994, doi:10.1117/1.JRS.8.084994.

809 Tian, B., D. E. Waliser, E. J. Fetzer, and Y. L. Yung (2010), Vertical moist
810 thermodynamic structure of the Madden-Julian oscillation in atmospheric infrared
811 sounder retrievals: An update and a comparison to ECMWF interim re-analysis,
812 Mon. Weather Rev., 138 (12), 4576-4582, ISSN 0027-0644.

813 Vonder Haar, T.H., J.L. Bytheway, and J.M. Forsythe (2012) Weather and climate
814 analyses using improved global water vapor observations, Geophys. Res. Lett., 39,
815 L15802, doi: 10.1029/20122GL052094.

816 Wong, T., B. A. Wielicki, R. B. Lee, III, G. L. Smith, K. A. Bush, J. K. Willis (2006),
817 Reexamination of the observed decadal variability of the Earth Radiation Budget
818 using altitude-corrected ERBE/ERBS nonscanner WFOV data, J. Clim., 19, 4028-4040.

819 Zelinka, M. D. and D. L. Hartmann (2011), The observed sensitivity of high clouds to
820 mean surface temperature anomalies in the tropics, J. Geophys. Res., 116, D23103,
821 doi: 10.1029/2011JD016459.

822 Zelinka, M. D., S. A. Klein, and D. L. Hartmann (2012a), Computing and partitioning
823 cloud feedbacks using cloud property histograms. Part 1: Cloud radiative kernels, J.
824 Clim., 25, 3715–3735, doi: 10.1175/JCLI-D- 11-00248.1.

825 Zelinka, M. D., S. A. Klein, and D. L. Hartmann (2012b), Computing and partitioning
826 cloud feedbacks using cloud property histograms. Part 2: Attribution to the nature
827 of cloud changes, J. Clim., 25, 3736–3754, doi:10.1175/JCLI-D-11-00249.1.

828

829 Table 1

830

	AIRS 1:30 AM minus CERES	AIRS 1:30 PM minus CERES	AIRS 1:30 AM/PM minus CERES
Global Mean			
Bias	-0.25	6.22	2.99
STD	0.22	0.38	0.25
Slope ($W/m^2/yr$)	0.0018±0.0085	-0.0068± 0.0145	-0.0028±0.0094
Tropical Mean			
Bias	-0.21	7.62	3.71
STD	0.32	0.42	0.27
Slope ($W/m^2/yr$)	0.0054±0.0122	-0.0080±0.0158	-0.0017±0.0102
30N-90N Mean			
Bias	-1.34	6.18	2.42
STD	0.73	1.15	0.37
Slope ($W/m^2/yr$)	-0.0118±0.0277	-0.0022±0.0438	-0.0072±0.0142
30S-90S Mean			
Bias	-0.75	3.46	2.11
STD	0.90	0.45	0.33
Slope ($W/m^2/yr$)	0.0082±0.0344	-0.0089±0.0171	-0.0007±0.0126

831

832

833 Table 2

	Global Mean	Tropical Mean	N. Hemisphere Extra-tropics	S. Hemisphere Extra-tropics
AIRS 1:30 PM	0.0024±0.0189	-0.0163±0.0361	0.0432±0.0406	-0.0008±0.0257
AIRS 1:30 AM	0.0110±0.0163	-0.0029±0.0312	0.0510±0.0343	-0.0012±0.0261
AIRS 1:30 AM/PM	0.0064±0.0174	-0.0100±0.0335	0.0469±0.0370	-0.0013±0.0256
CERES	0.0112±0.0179	-0.0063±0.0345	0.0554±0.0366	0.0020±0.0259

834

835

836 Table A1

837

Band Number	Frequency Range	Clear Sky OLR		OLR		LWCRF	
		Flux	%	Flux	%	Flux	%
1	100-350	34.79	13.03	34.40	14.14	0.39	1.65
2	350-500	42.90	16.06	40.97	16.84	1.93	8.09
3	500-630	38.94	14.58	36.46	14.99	2.48	10.41
4	630-700	10.27	3.85	10.26	4.22	0.01	0.06
5	700-820	32.37	12.12	29.04	11.94	3.33	13.96
6	820-980	46.77	17.51	39.89	16.40	6.88	28.83
7	980-1080	16.88	6.32	14.50	5.96	2.37	9.96
8	1080-1180	17.69	6.62	14.73	6.05	2.97	12.44
9	1180-1390	17.13	6.41	14.70	6.04	2.43	10.20
10	1390-1480	2.43	0.91	2.26	0.93	0.17	0.72
11	1480-1800	2.95	1.10	2.78	1.14	0.17	0.70
12	1800-2080	2.37	0.89	2.01	0.83	0.36	1.53
13	2080-2250	0.79	0.30	0.63	0.26	0.16	0.69
14	2250-2380	0.05	0.02	0.05	0.02	0.00	0.00
15	2380-2600	0.44	0.16	0.34	0.14	0.10	0.44
16	2600-3260	0.34	0.13	0.25	0.10	0.08	0.34

838

839

Figure and Table Captions

Table 1:

Area mean values of the mean difference (AIRS OLR minus CERES OLR), and standard deviation (STD) of the differences, for each of the three sets of AIRS OLR, as well as the slopes of the linear least squares fit to the differences between AIRS and CERES OLR ($W/m^2/yr$) for the period September 2002 through August 2016. The uncertainties of the slopes are twice the STDs of the linear least squares fits to the time series of differences.

Table 2:

Area mean AIRS and CERES OLR ARCs ($W/m^2/yr$). The uncertainties of the ARCs are twice the STDs of the linear least squares fits to the anomaly time series.

Table A1:

Frequency ranges of the spectral bands used to compute AIRS OLR global mean annual mean band fluxes (W/m^2), and the percentage contribution of each band to Clear Sky OLR, OLR, and LWCRF.

Figure 1

Monthly mean area mean AIRS and CERES OLR time series data from September 2002 through August 2016 over four spatial domains: global; the Northern Hemisphere extra-tropics; the tropics; and Southern Hemisphere extra-tropics. The vertical black lines indicate January of each year.

Figure 2

The differences (AIRS minus CERES) of area mean OLR time series from September 2002 through August 2016 over the same four spatial domains shown in Figure 1.

Figure 3

AIRS and CERES monthly mean January OLR climatologies and climatological differences on a 1°x1° spatial scale. The statistics under each figure indicate the area weighted global mean (GM) value of the field and the area weighted spatial standard deviation (STD).

Figure 4

AIRS and CERES monthly mean July OLR climatologies and climatological differences on a 1°x1° spatial scale.

Figure 5

AIRS day minus night climatological differences of Surface Skin Temperature, Radiative Effective Cloud Fraction, and 500 mb Specific Humidity for January and July.

Figure 6

AIRS and CERES monthly mean area mean OLR anomaly time series from September 2002 through August 2016 over four spatial domains: global; the Northern Hemisphere extra-tropics; the tropics; and the Southern Hemisphere extra-tropics. The tropical OLR anomaly time-series also shows monthly mean values of the El Niño Index.

Figure 7

ARCs ($W/m^2/yr$) and ENCs of $AIRS_{AVG}$ OLR and CERES OLR over the time-period September 2002 through August 2016. The NOAA Niño-4 region is outlined in black, and the NOAA Niño-3 region is outlined in gray, in this figure as well as in some subsequent figures.

Figure 8

Spatial 1˚ latitude by 1˚ longitude distributions of ARCs of $AIRS_{AVG}$ Surface Skin Temperature, Surface Air Temperature, 500 mb Specific Humidity, and Radiative Effective Cloud Fraction over the time period September 2002 through August 2016.

905 Figure 9

906 Spatial 1˚ latitude by 1˚ longitude distributions of ENCs of $AIRS_{AVG}$ Surface Skin
907 Temperature, Surface Air Temperature, 500 mb Specific Humidity, and Radiative
908 Effective Cloud Fraction over the time-period September 2002 through August 2016.

909

910 Figure 10

911 Hovmöller diagrams of $AIRS_{AVG}$ monthly mean anomaly time-series integrated over
912 the latitude range 5˚N through 5˚S (vertical scale) in each 1˚ longitude bin
913 (horizontal scale), for the period September 2002 through August 2016. a) Surface
914 Skin Temperature (K), b) OLR (W/m^2), c) 500 mb Specific Humidity (g/kg), d)
915 Radiative Effective Cloud Fraction (%).

916

917 Figure 11

918 ARCs over the time-period September 2002 through August 2016 of AIRS 1:30 PM
919 Surface Skin Temperature, AIRS 1:30 AM Surface Skin Temperature, AIRS 1:30 PM
920 minus 1:30 AM Surface Skin Temperature, and AIRS 1:30 PM minus 1:30AM 500 mb
921 Specific Humidity.

922

923 Figure 12

924 ENCs over the time-period September 2002 through August 2016 of AIRS 1:30 PM
925 Surface Skin Temperature, AIRS 1:30 AM Surface Skin Temperature, AIRS 1:30 PM
926 minus 1:30 AM Surface Skin Temperature, and AIRS 1:30 PM minus 1:30 AM 500
927 mb Specific Humidity.

928

929 Figure 13

930 Monthly mean Surface Skin Temperature anomaly time series averaged over
931 Eastern Australia for the time period September 2002 through August 2016 a)1:30
932 PM, b)1:30 AM, and c)1:30 PM minus 1:30 AM. Also shown on each figure is twice
933 the ENI.

934

Figure 1.

Area Mean OLR Time Series (W/m^2)
September 2002 through August 2016
Global

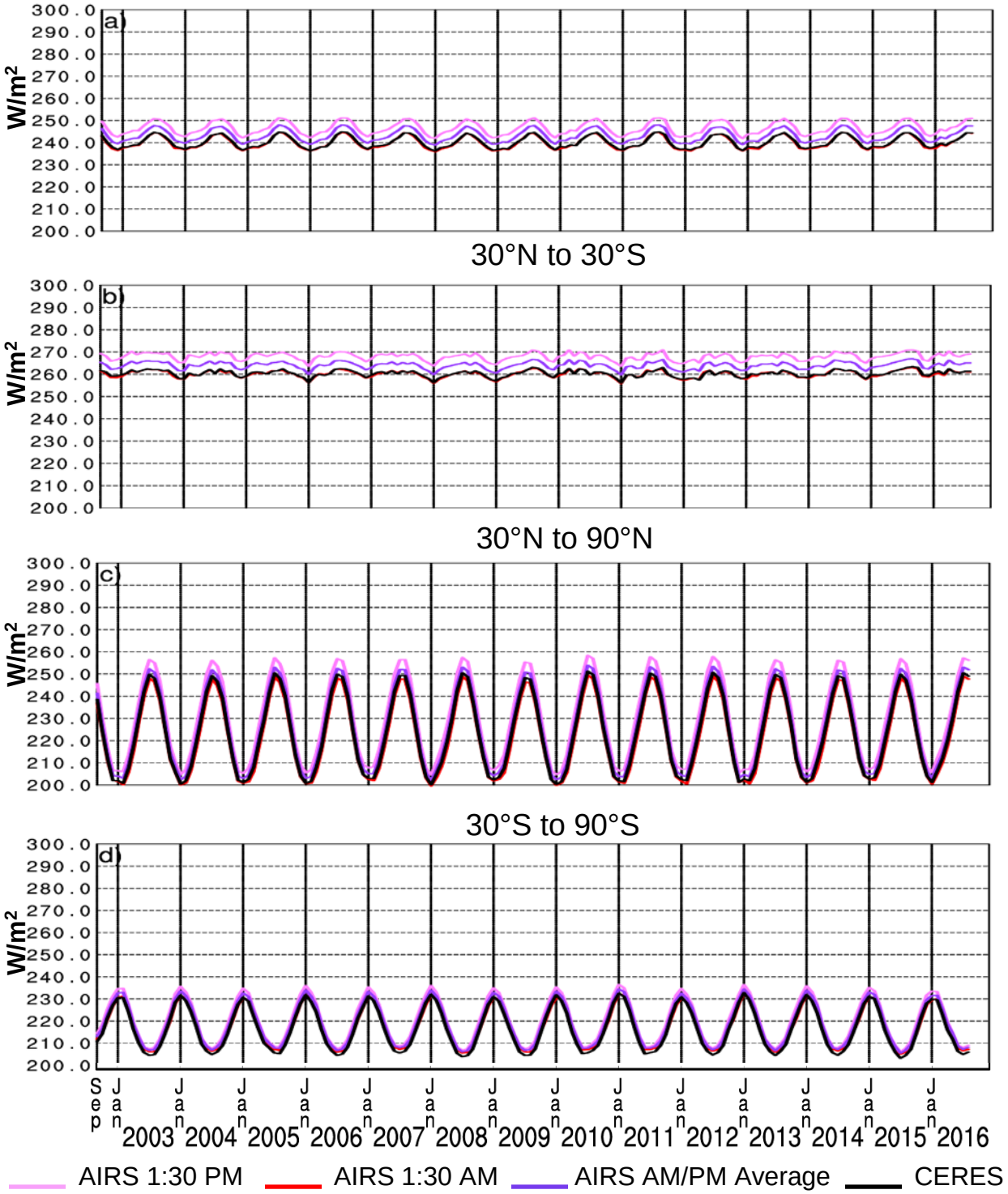

Figure 2.

Area Mean OLR Time Series Differences from CERES (W/m^2)
September 2002 through March 2016

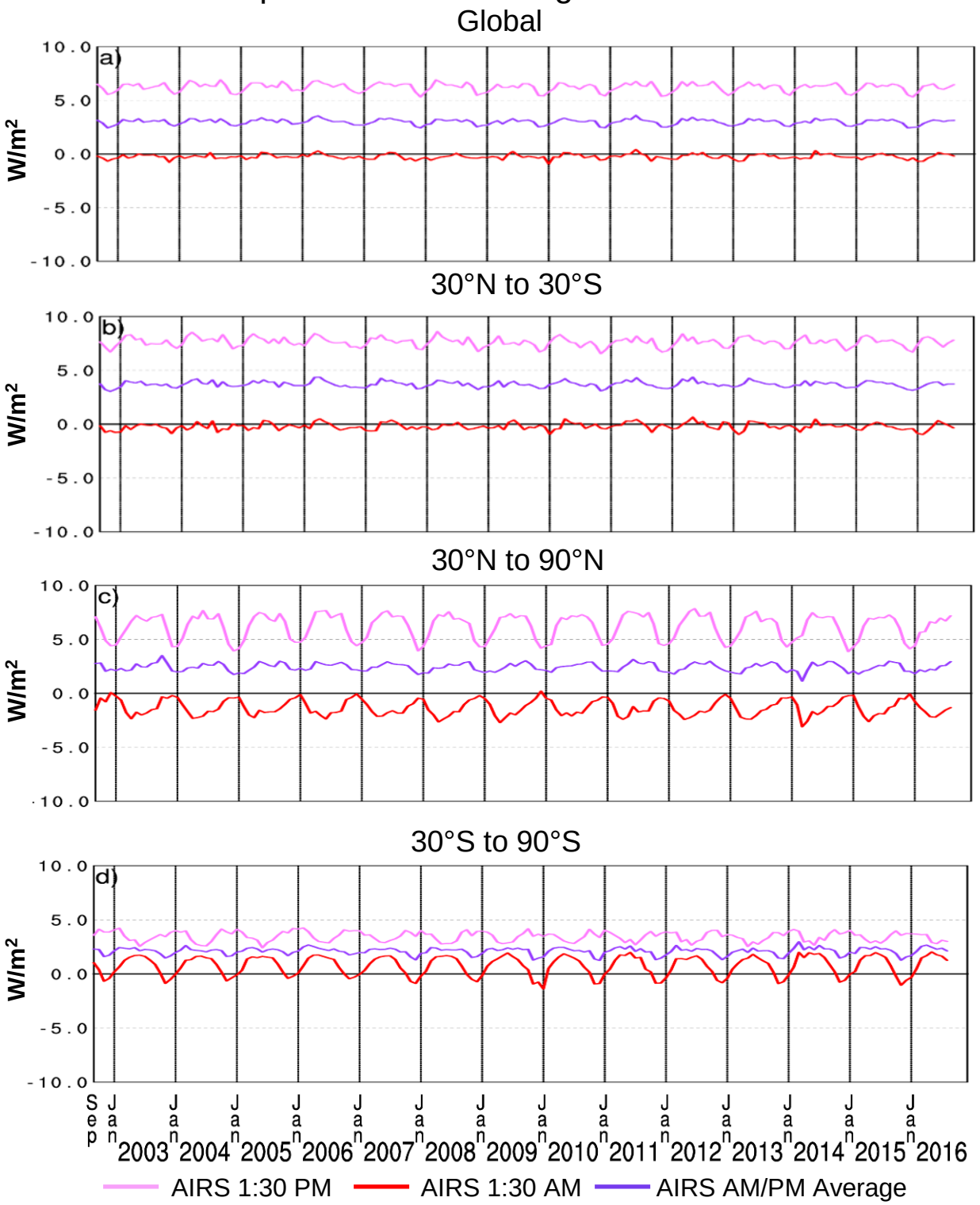

Figure 3.

Outgoing Longwave Radiation (W/m^2)
January Climatology

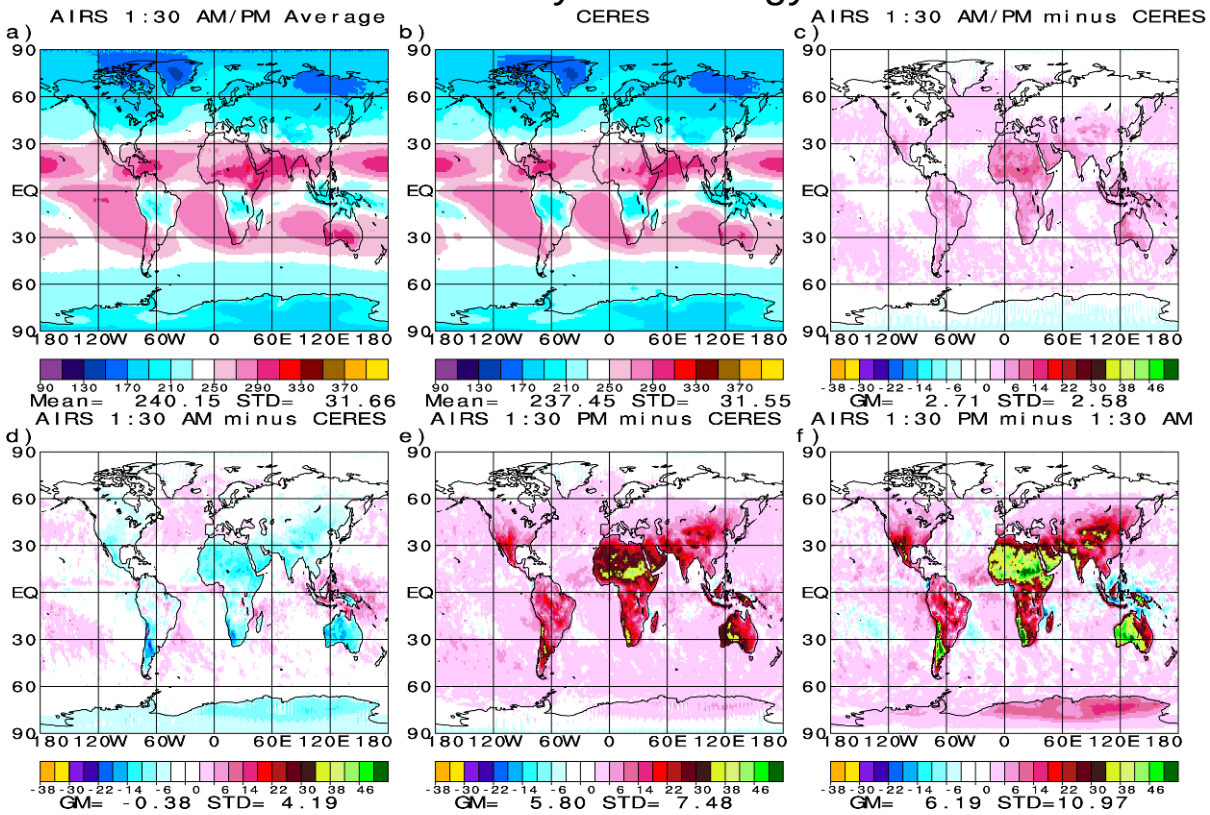

Figure 4.

Outgoing Longwave Radiation (W/m^2)
July Climatology

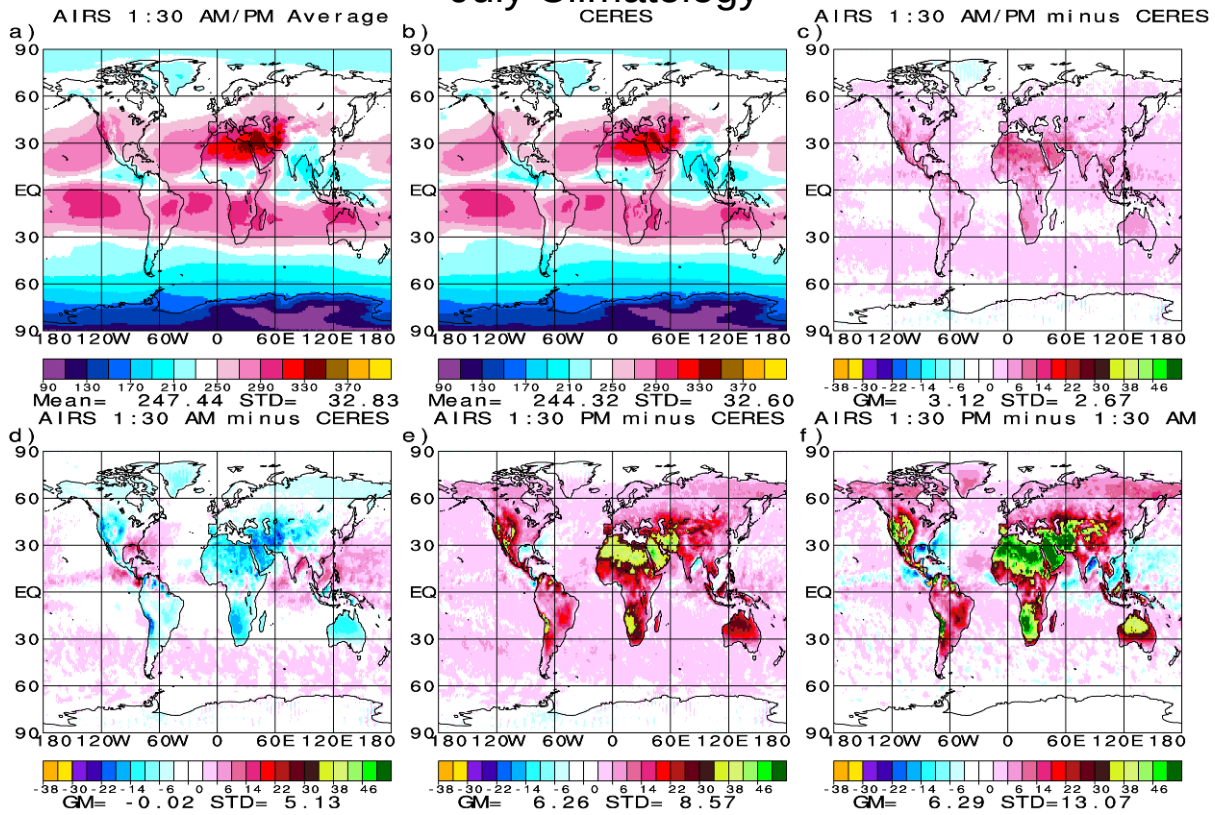

Figure 5.

1:30 PM minus 1:30 AM Climatological Differences

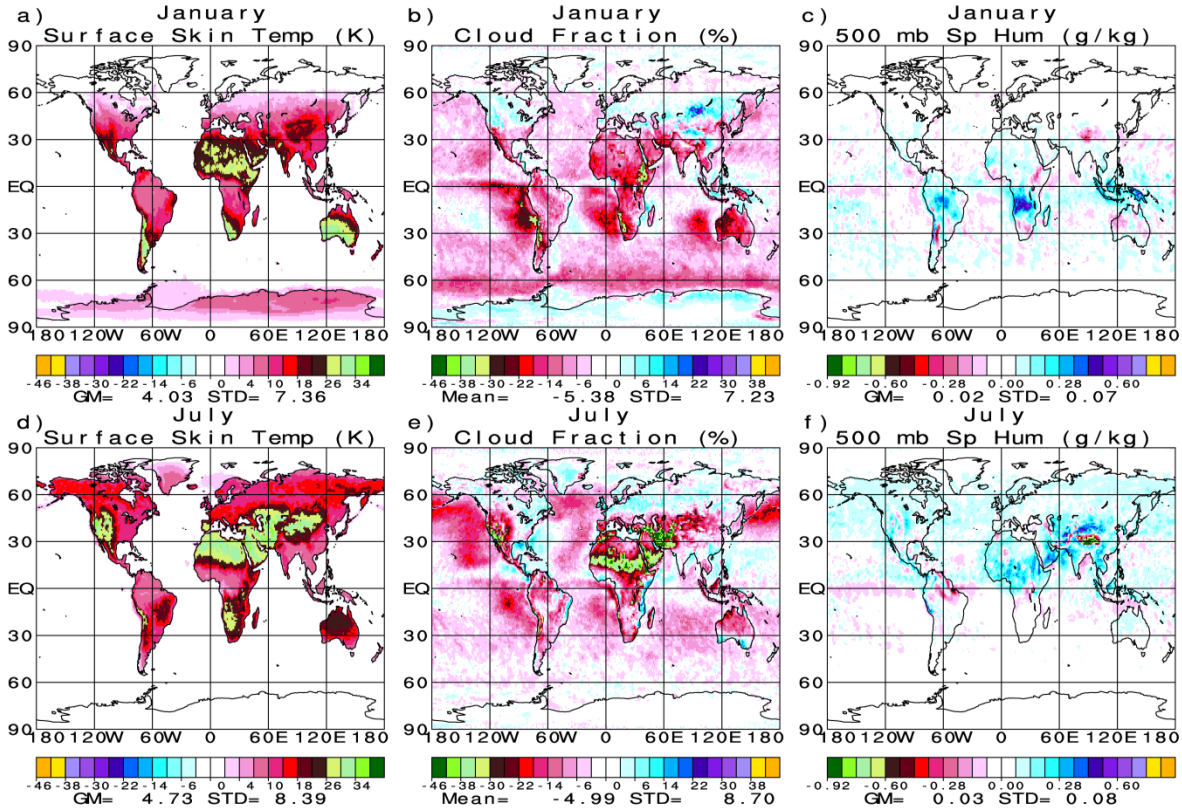

Figure 6.

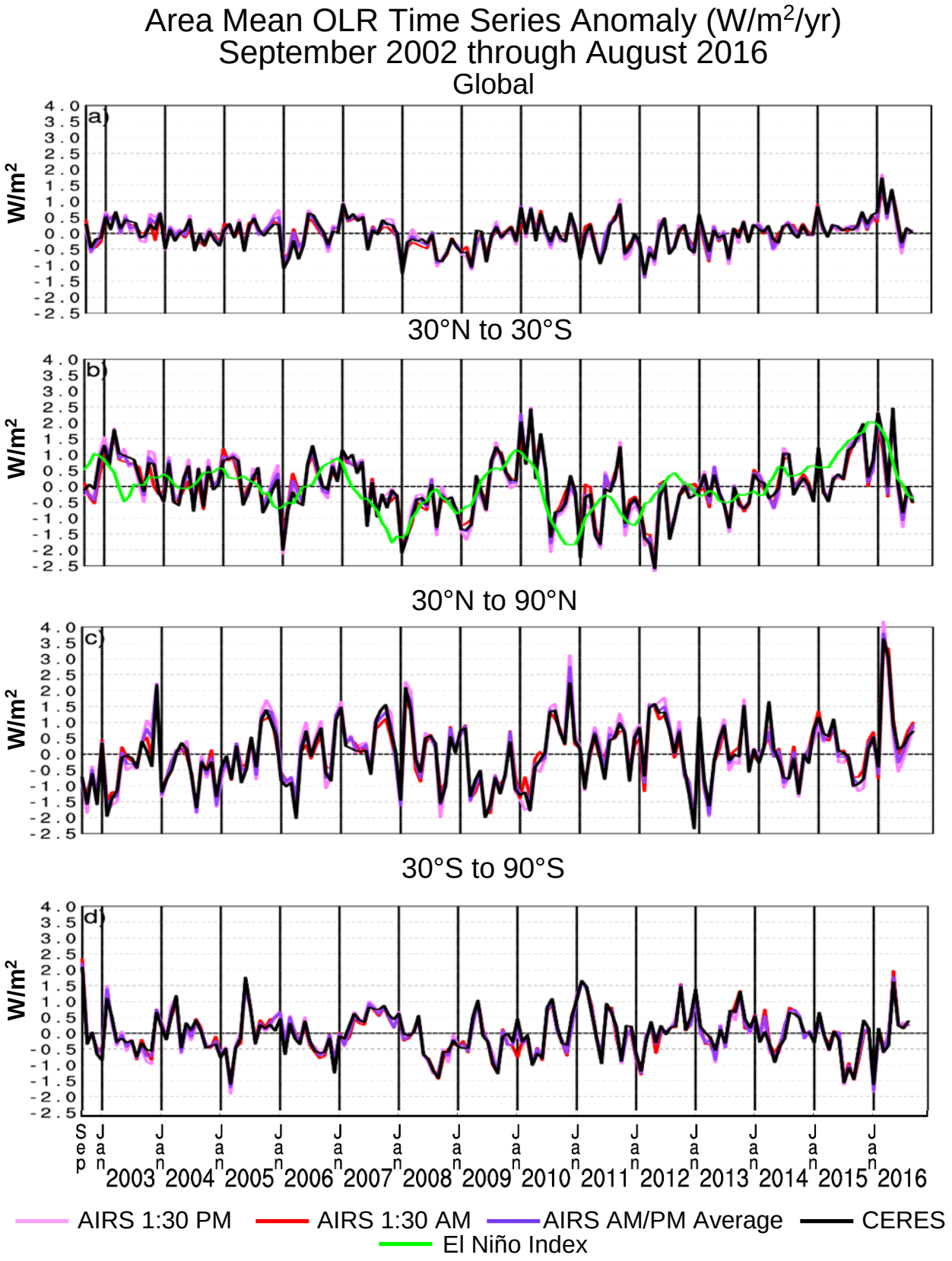
Area Mean OLR Time Series Anomaly (W/m2/yr)
September 2002 through August 2016
Global
a)
W/m2
30°N to 30°S
b)
W/m2
30°N to 90°N
c)
W/m2
30°S to 90°S
d)
W/m2
Sep
Jan
2003
2004
2005
2006
2007
2008
2009
2010
2011
2012
2013
2014
2015
2016
AIRS 1:30 PM
AIRS 1:30 AM
AIRS AM/PM Average
CERES
El Niño Index

Figure 7.

OLR ARC's (W/m^2/yr) September 2002 through August 2016

a) AIRS Average

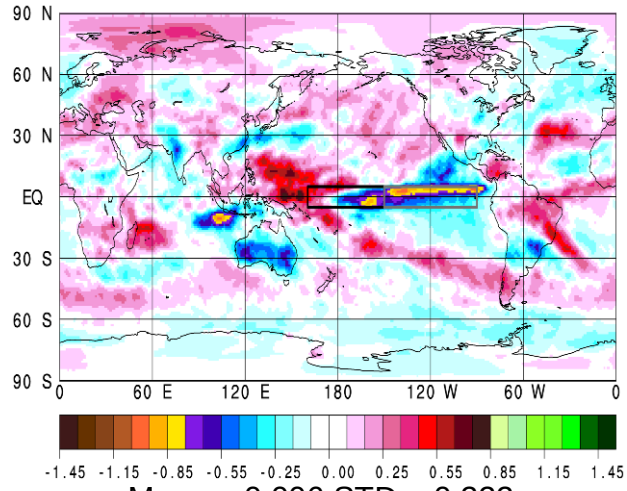

Mean = 0.006 STD = 0.222

b) CERES

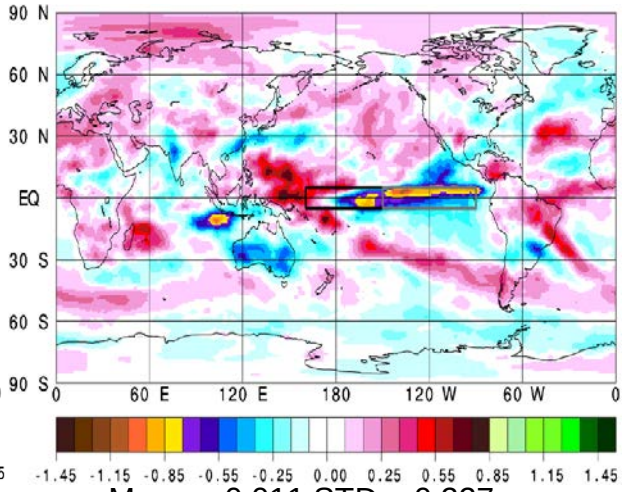

Mean = 0.011 STD = 0.227

c) AIRS Average minus CERES

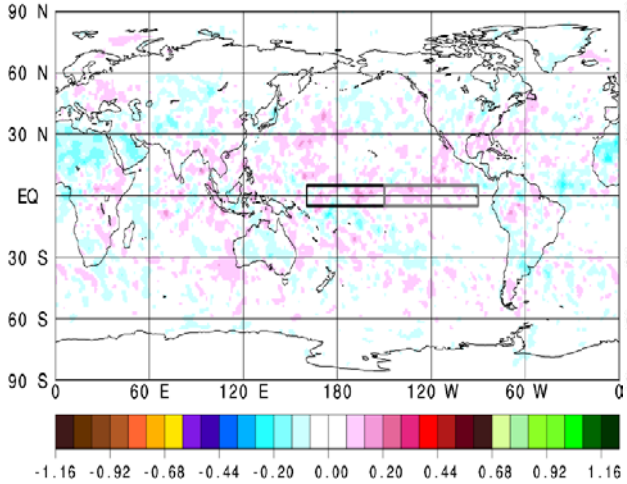

Mean = -0.005 STD = 0.047 Cor= 0.978

d) AIRS 1:30 PM minus 1:30 AM

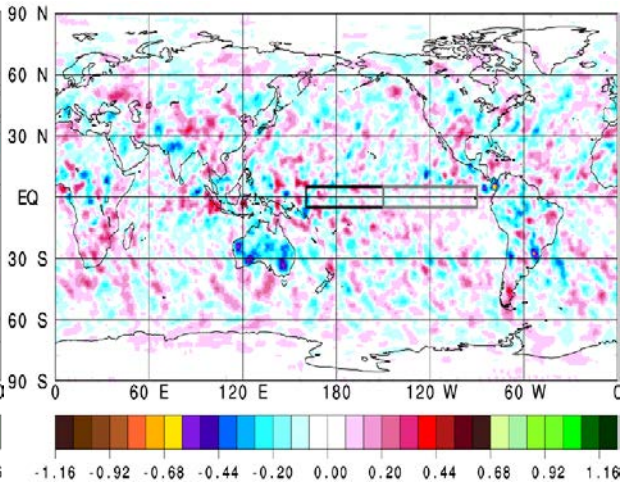

Mean = -0.009 STD = 0.116 Cor= 0.871

OLR ENC's September 2002 through August 2016

e) AIRS Average

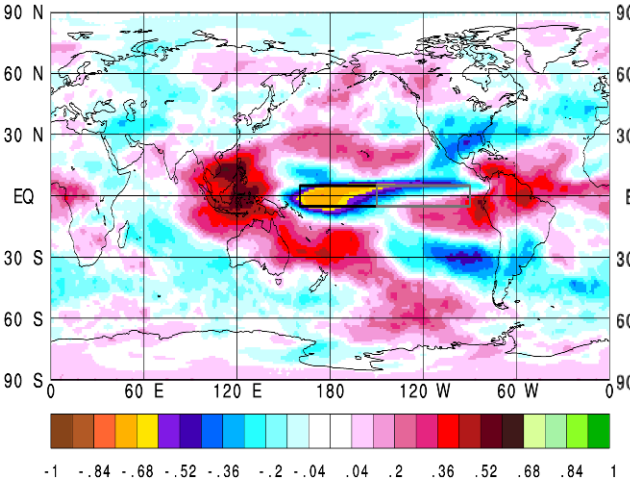

Mean = 0.010 STD = 0.222

f) CERES

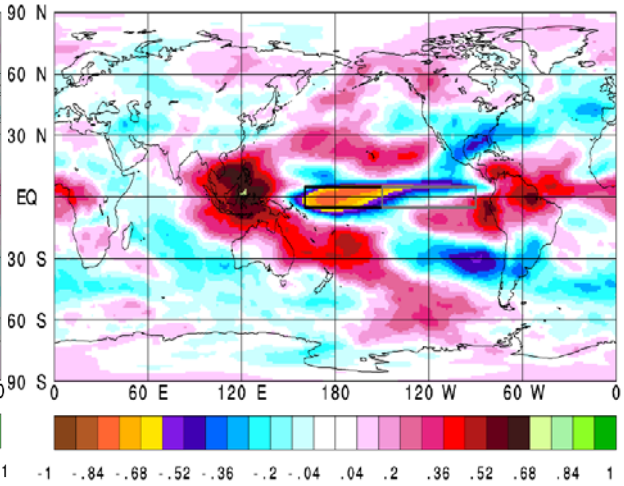

Mean = 0.013 STD = 0.243

Figure 8.

AIRS Average ARC's September 2002 through August 2016

a) Surface Skin Temperature (K/yr)

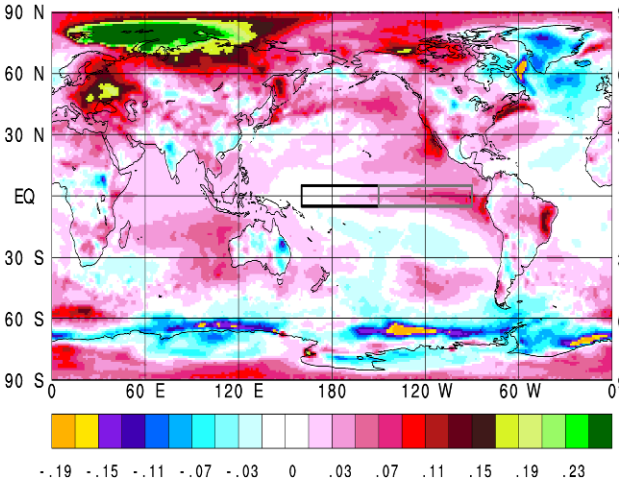

Mean = 0.019 STD = 0.036

b) Surface Air Temperature (K/yr)

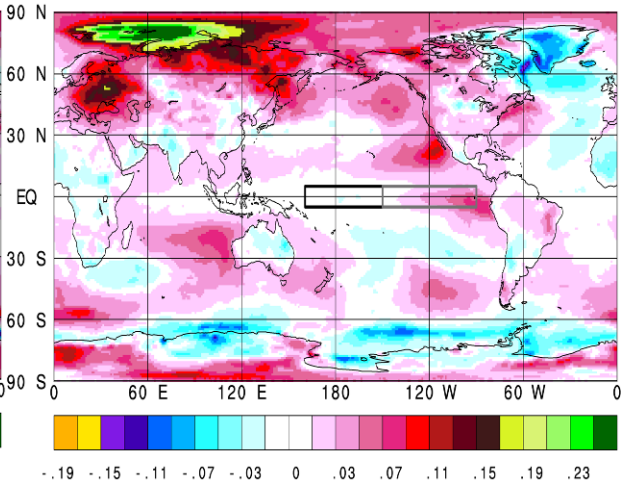

Mean = 0.016 STD = 0.029

c) 500 mb Specific Humidity (g/kg/yr)

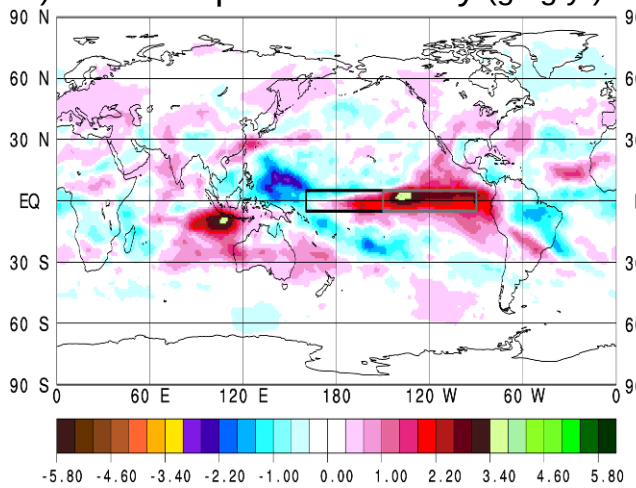

Mean = 0.066 STD = 0.709

d) Cloud Fraction (%/yr)

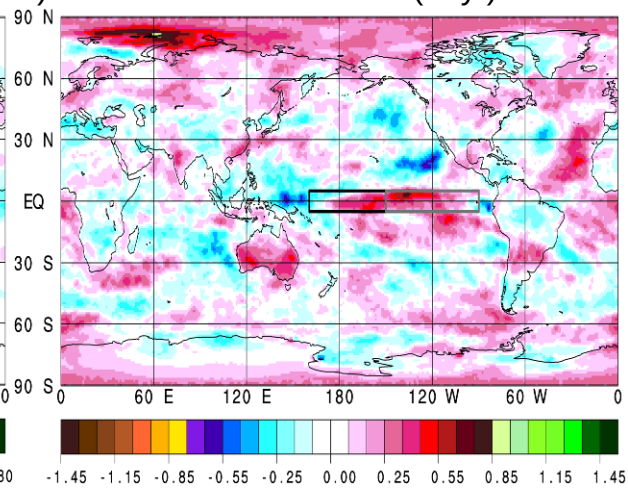

Mean = 0.023 STD = 0.161

Figure 9.

AIRS Average ENC's September 2002 through August 2016

a) Surface Skin Temperature

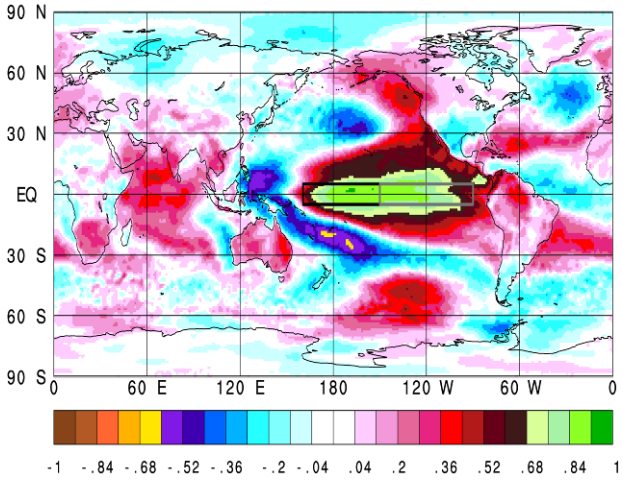

Mean = 0.08 STD = 0.28

b) Surface Air Temperature

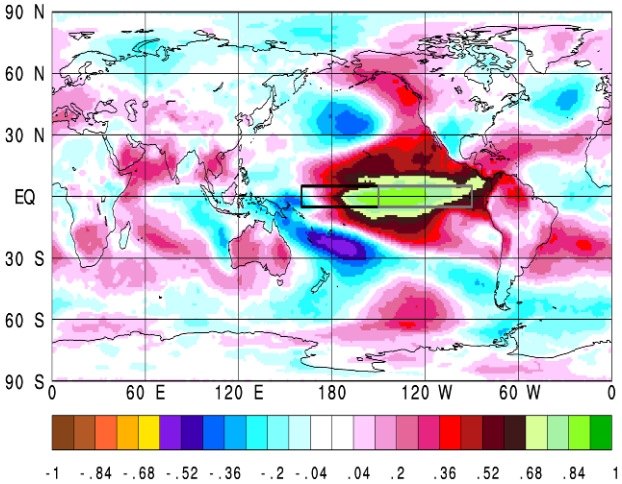

Mean = 0.07 STD = 0.25

c) 500 mb Specific Humidity

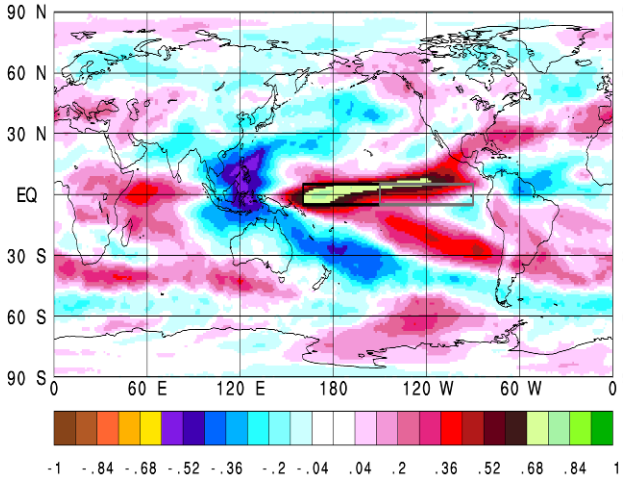

Mean = 0.02 STD = 0.22

d) Cloud Fraction

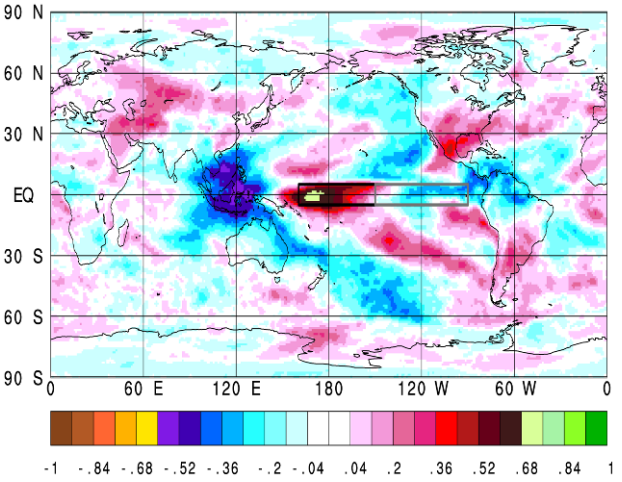

Mean = -0.02 STD = 0.18

Figure 10.

AIRS Anomalies Tropics 5°N to 5°S September 2002 through August 2016

a) Surface Skin Temperature (K)

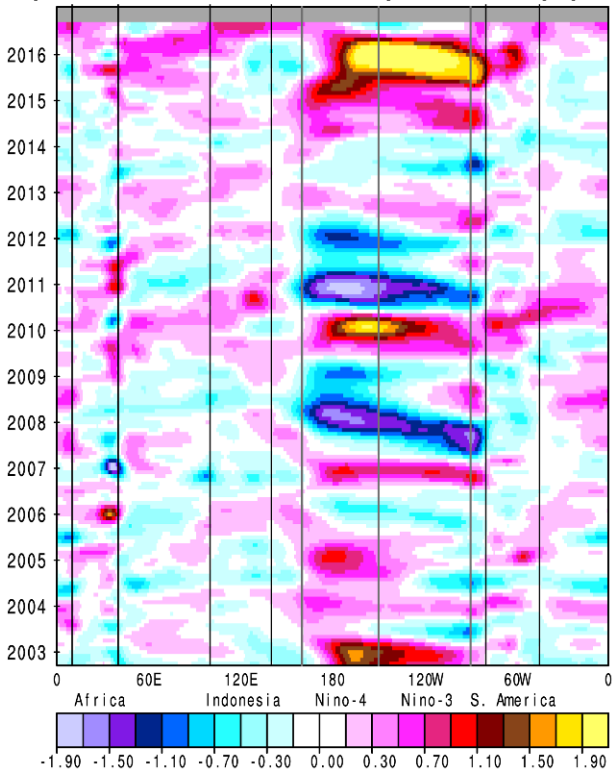

b) OLR (W/m^2)

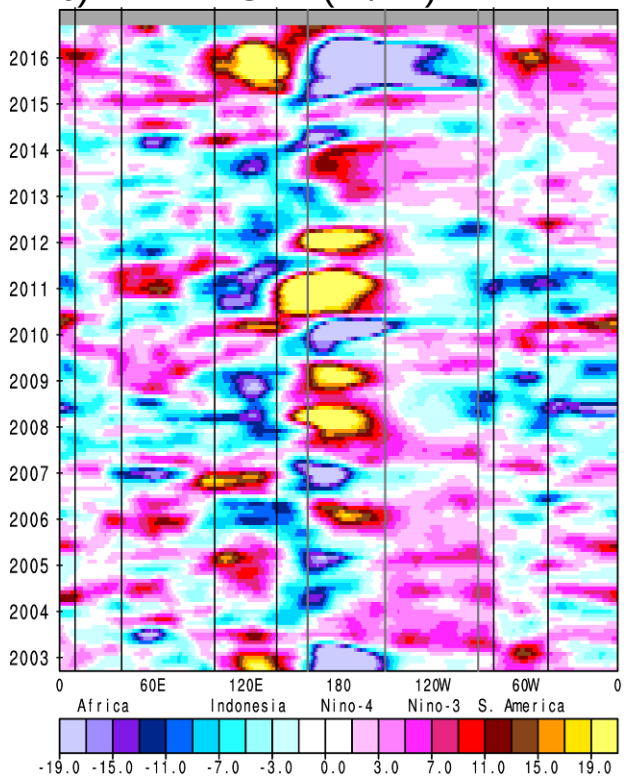

c) 500 mb Specific Humidity (g/kg)

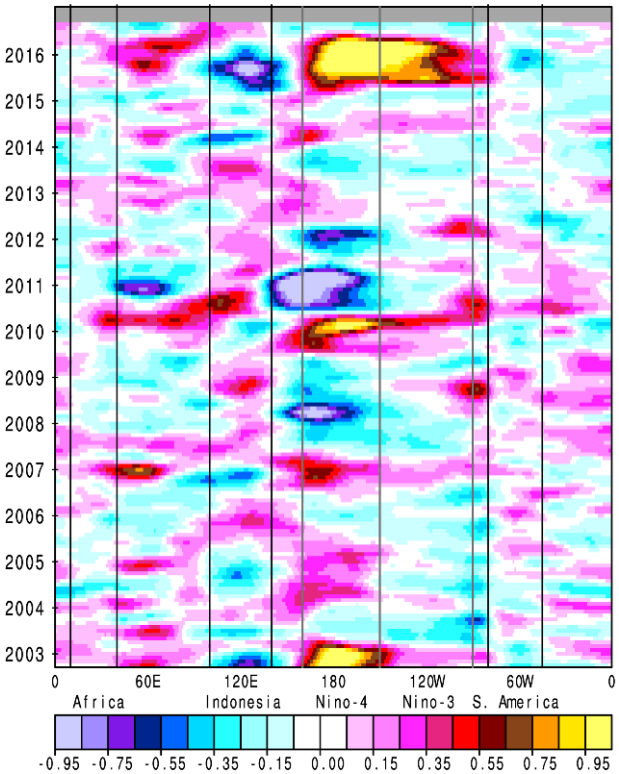

d) Cloud Fraction (%)

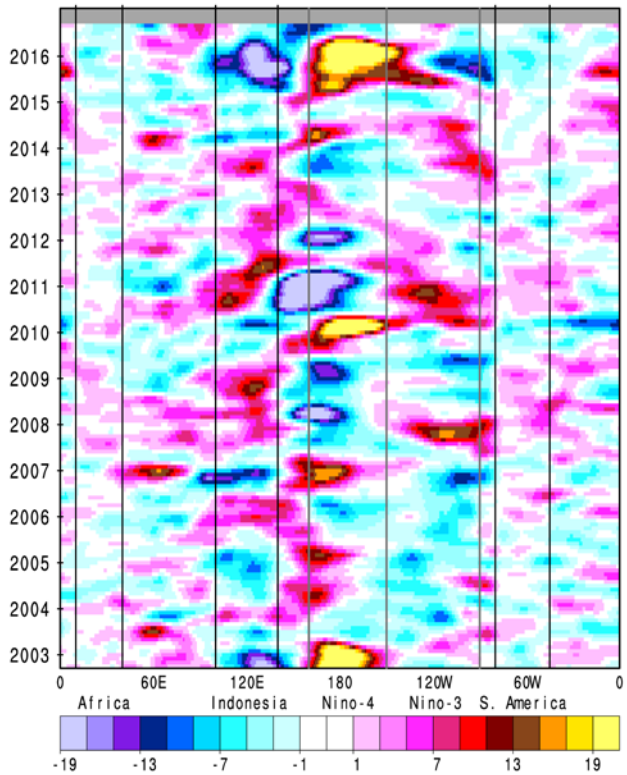

Figure 11.

AIRS ARC's September 2002 through August 2016

a) Surface Skin Temperature (K/yr) 1:30 PM

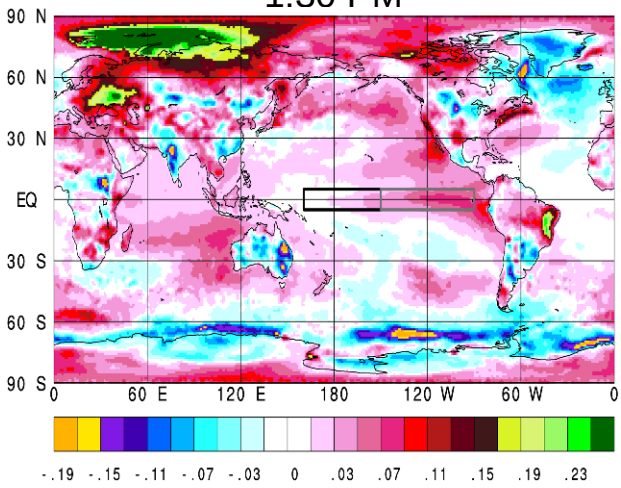

Mean = 0.019 STD = 0.041

b) Surface Skin Temperature (K/yr) 1:30 AM

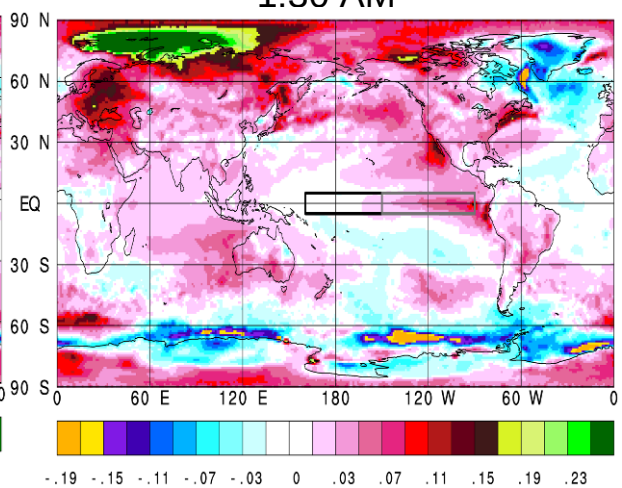

Mean = 0.019 STD = 0.035

c) Surface Skin Temperature (K/yr) PM minus AM

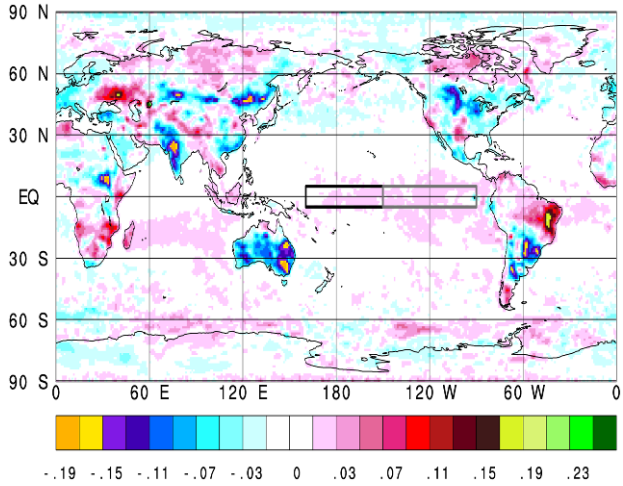

Mean = 0.000 STD = 0.027

d) 500 mb Specific Humidity (g/kg/yr) PM minus AM

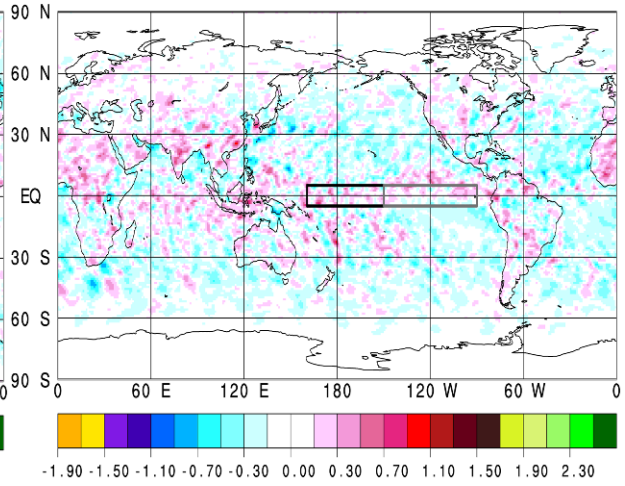

Mean = -0.053 STD = 0.209

Figure 12.

AIRS ENC's September 2002 through August 2016

a) Surface Skin Temperature
1:30 PM

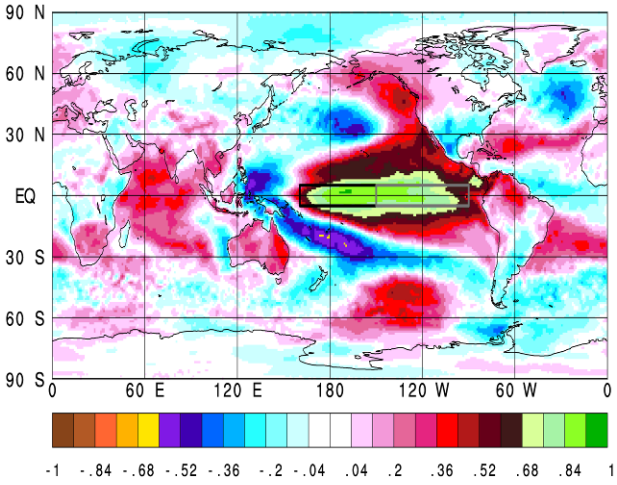

Mean = 0.08 STD = 0.28

b) Surface Skin Temperature
1:30 AM

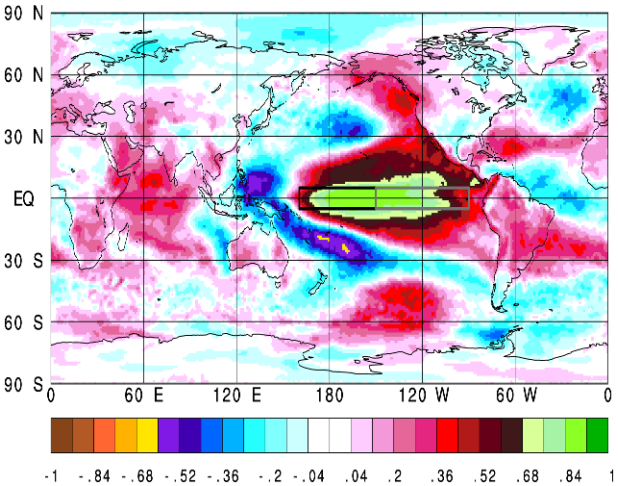

Mean = 0.08 STD = 0.028

c) Surface Skin Temperature
PM minus AM

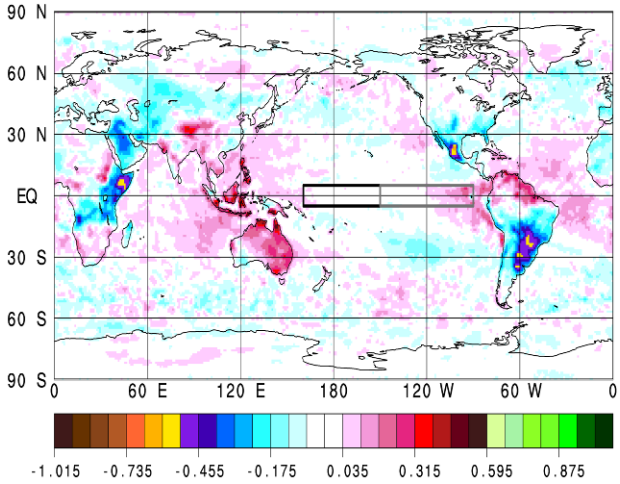

Mean = 0.00 STD = 0.01

d) 500 mb Specific Humidity
PM minus AM

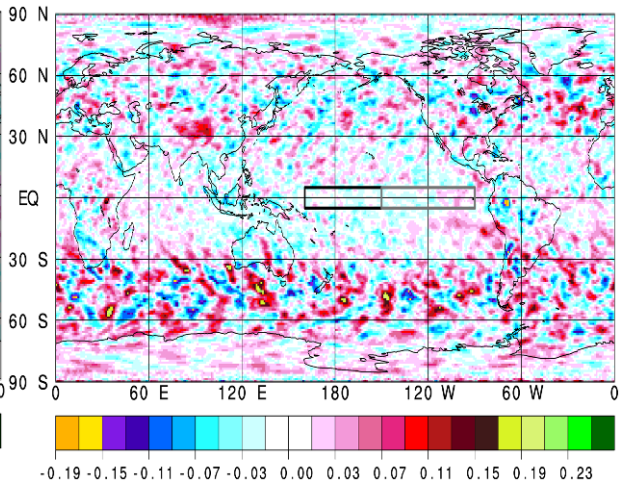

Mean = 0.00 STD = 0.04

Figure 13.

Surface Skin Temperature Time Series Anomaly (K/yr)
Eastern Australia September 2002 through August 2016